Conceptual design and performance study for the first implementation of AGATA at the in-flight RIB facility of GSI

C. Domingo-Pardo [a,b,*], D. Bazzacco [c], P. Doornenbal [d], E. Farnea [c], A. Gadea [a], J. Gerl [b], H.J. Wollersheim [b]

[a] IFIC, CSIC-University of Valencia, Valencia, Spain
[b] GSI Helmholtzzentrum für Schwerionenforschung GmbH, Darmstadt, Germany
[c] Istituto Nazionale di Fisica Nucleare, Sezione di Padova, Italy
[d] RIKEN, Japan

The AGATA Collaboration

ARTICLE INFO

ABSTRACT

The main objective of the Advanced GAmma Tracking Array (AGATA) is the investigation of the structure of exotic nuclei at the new generation of RIB facilities. As part of the preparatory phase for FAIR-NUSTAR, AGATA is going to be installed at the FRS fragmentation facility of the GSI centre for an experimental campaign to be performed in 2012 and 2013. Owing to its γ-ray tracking capabilities and the envisaged enhancement in resolving power, a series of in-flight γ-ray spectroscopy experiments are being planned. The present work describes the conceptual design of this first implementation of AGATA at GSI-FRS, and provides information about the expected performance figures. According to the characteristics of each particular experiment, it is foreseen that the target–array distance is adjusted in order to achieve the optimum compromise between detection efficiency and energy resolution, or to cover an specific angular range of the emitted electromagnetic radiation. Thus, a comprehensive Monte Carlo study of the detection sensitivity in terms of photopeak efficiency, resolution and peak-to-total ratio, as a function of the target–array distance is presented. Several configurations have been investigated, and MC-calculations indicate that a remarkable enhancement in resolving power can be achieved when double-cluster AGATA detectors are developed and implemented. Several experimental effects are also investigated. This concerns the impact of passive materials between the target and the array, the angular distribution of the detection efficiency and the influence of target thickness effects and transition lifetimes in the attainable detection sensitivity. A short overview on half-life measurements via lineshape effects utilizing AGATA is also presented.

1. Introduction

The study of nuclear structure far-off stability benefits from advances in both, acceleration techniques, as well as in detection systems. Since their invention in 1960, semiconductor germanium detectors represent key instruments in the field of high-resolution γ-ray spectroscopy. The unsurpassed energy resolution of germanium detectors has led to the discovery of new features and astounding properties of the atomic nucleus. Developments such as Ge-arrays like EUROBALL [1] and GAMMASPHERE [2] led to about two orders of magnitude improvement in resolving power when compared to the first generation of Compton-suppression arrays like HERA [3] or TESSA3 [4]. Remarkable results were, for example, the measurement of superdeformed nuclei with very high-angular-momentum states [5–7], thus revealing nuclear rotating systems with moments of inertia larger than 80 $\hbar^2$ MeV^{-1}.

At present, the hot topics of nuclear structure with Radioactive Ion Beams (RIBs) concern the evolution of shell gaps and the related changes in magic numbers far-off stability; breakdown of isospin symmetry and its interplay with nuclear shape evolution and shape coexistence phenomena; determination of the drip-line border of the nuclei chart and its link to open quantum systems, that in turn allow for understanding the coupling between bound states and the continuum; collectivity phenomena and electric and magnetic strength in nuclei, including also the investigation of giant resonances, as well as the fine structure in the Pygmy Dipole Resonance [8]. A deeper understanding of these scientific themes will become possible in the near future thanks to the combination of more exotic RIBs with state-of-the-art γ-ray

detection systems. The latter concern the concept of γ-ray tracking. Owing to this novel approach, new generation arrays of 2D-segmented 3D-position sensitive detectors, such as the Advanced GAmma Tracking Array (AGATA) in Europe [9] and the Gamma-Ray Energy Tracking Array (GRETA) in USA [10] are being developed and early implementations are already used for in-beam γ-ray spectroscopy experiments.

Following a research and development phase including Monte Carlo simulations and design studies [11–17], detector character-ization [18–25], technical developments [26,27,9], as well as a commissioning and in-beam test of the system [28–36], the first sub-array of AGATA, the so-called AGATA Demonstrator, has been successfully set-up in operation at the stable ion beam facility of Laboratori Nazionali di Legnaro LNL-INFN (Italy) [37].

In order to exploit the complementarity offered by the different facilities in Europe, AGATA has been conceived as a peripatetic apparatus, travelling from one facility to another. Thus, the next experimental campaign of the next AGATA con-struction phase will be carried out, during 2012 and 2013, at the GSI centre for heavy ion research (Germany) in the framework of PreSPEC [38], which represents the preparatory phase for HISPEC/DESPEC at FAIR. HISPEC and DESPEC, which stand, respectively, for High-resolution In-flight SPECtroscopy and DEcay SPECtro-scopy experiments, will be part of the NUSTAR (NUclear STruc-ture, Astrophysics and Reactions) collaboration, the major next generation in-flight RIB facility in Europe. Similar to the existing site at GSI, FAIR-NUSTAR will be based on the production of fragments from 0.4 to 1 GeV/u beams and their separation in the Super-FRS [39,40]. The forthcoming installation of AGATA at GSI-FRS will benefit from improvements in the beam intensities, which are a consequence of present accelerator developments towards FAIR. However, there are a number of relevant differ-ences in the experimental conditions of GSI-FRS when compared to the previous host, INFN-LNL, which need to be taken into account. Such particularities concern mainly the relativistic momentum (typically $\beta \sim 0.43$) and the spatial distribution (FWHM$_X \sim 6$ cm) of the RIB at GSI-FRS, when compared to the narrow (FWHM$_X \sim 2$ mm) stable beams, commonly used at INFN-LNL with lower beam velocities (e.g. $\beta \lesssim 0.1$). Thus, in order to optimize its γ-ray efficiency and high intrinsic energy- and spatial-resolution, the configuration of the AGATA detectors needs to be designed according to the characteristics of the ion beam at the final focal plane of the GSI fragment separator (FRS). With this purpose, systematic Monte Carlo (MC) simulations have been performed and their results are reported in this paper. Section 2 summarizes the general features of the fragmentation facility at GSI, and the typical experimental conditions for in-flight γ-ray spectroscopy experiments using relativistic beams, with particular emphasis on the main differences in the experi-mental conditions with respect to the previous AGATA campaign, hosted at LNL-INFN.

The original design of AGATA [14] is based on n-type HPGe crystals, which have a tapered hexagonal geometry with an asym-metric shape to fit into the 4π 180 detector geometry. Such a geometry is realized by means of three different shapes, with a triplet of crystals arranged in identical triple cryostats. However, MC-simulations reported in Section 3 illustrate the need for devel-oping additional cluster detectors with only two crystals inside one cryostat. In the following, they will be referred to as AGATA double-cluster (ADC) detectors. Such development should allow for an optimal use of AGATA for in-flight measurements using the RIBs available at GSI-FRS, as well as for the HISPEC experiment in the future FAIR-NUSTAR facility. Section 4 describes the attainable γ-ray detection sensitivity for such hybrid AGATA-shell geometries, with a variable number of double- and triple-cluster detectors. This seems convenient because of the non-proportionality between efficiency

and number of capsules. Also, results reported in Section 4 demon-strate the potential to pick-up expected efficiency, resolution and peak-to-total (P/T) ratios, according to the number of cluster detectors available for the array at the time of each particular experiment. The performance of several combinations of double- and triple-cluster detectors, from 10 up to 40 capsules is displayed and tabulated. Photopeak efficiency, energy resolution and P/T ratios are represented as a function of the target–array distance, which can be adjusted for each particular experiment in order to find the best compromise according to the characteristics of the measurement.

The detection efficiency of AGATA varies with the γ-ray energy, which is also affected by the Lorentz boost. This depen-dency is reported in Section 5 for γ-quanta in the energy range from 500 keV up to 5 MeV and for several AGATA configurations. The Lorentz boost of the relativistic RIBs commonly used at GSI-FRS determines also, to a large extent, the angular distribution of the γ-ray detection efficiency. This relationship becomes of particular interest for a number of experiments (see e.g. [41]), as well as for the determination of reduced transition probabili-ties of excited states (see Section 9). Thus, Section 6 shows the angular variation of the photopeak efficiency for two AGATA configurations and for several target–array distances.

In the past campaigns with EUROBALL cluster detectors at GSI-FRS, a thin shielding made of lead was commonly utilized for reducing atomic backgrounds. The impact of such additional passive materials on the detection efficiency of AGATA is pre-sented in Section 7.

The impact of the half-life of the nuclear transition in combi-nation with target thickness effects is reported in Section 8. A short overview on half-life measurement via lineshape effects is described in Section 9.

2. The GSI fragmentation facility and experimental conditions

The production of RIBs at the GSI-FRS facility starts with a high intensity stable beam delivered by the UNILAC linear accelerator, and accelerated to relativistic energies by the SIS18 synchrotron. This primary beam impinges on a target at a high energy, typically between 400 MeV/u and 1 GeV/u. This way, a broad spectrum of radioactive species is produced by means of fragmentation or induced fission reactions. The production target is in most cases a Be- or a Pb-layer with a thickness between 2 and 4 g/cm². The fragments of interest are selected and transmitted through the fragment separator (FRS) using the $B\rho-\Delta E-B\rho$ method. A sche-matic layout of the experimental set-up is shown in Fig. 1. Ions are tracked through the FRS on an event-by-event basis. The mass-over-charge (A/Q) ratio is determined from the time-of-flight measured using two scintillators (Scintillator 1 and Scintil-lator 2 in Fig. 1). The charge of the ions is determined from their energy loss across two ionization chambers (MUSIC1 and MUSIC2). Two time-projection chambers (TPC1 and TPC2) are used to measure the position and the angle of the fragments arriving at the final focal plane of the FRS. A detailed description about the FRS can be found in Ref. [42].

The spatial profile of the fragments beam at the final focal plane of the FRS depends on several parameters, such as the beam energy and achromaticity. For energies of 100 MeV/u the beam shows a width of $\lesssim 6$ cm FWHM in the dispersive horizontal plane X and about 4 cm FWHM on the vertical axis Y (see Fig. 2).

A secondary target, typically with a size of 62.5×62.5 mm², is placed at the final FRS focal plane for inducing the reactions of interest in the impinging RIB. The target material is usually gold or lead for Coulomb excitation and beryllium for secondary fragmentation or particle knockout reactions. Thanks to the high secondary beam energy (~ 100 MeV/u) rather thick targets of
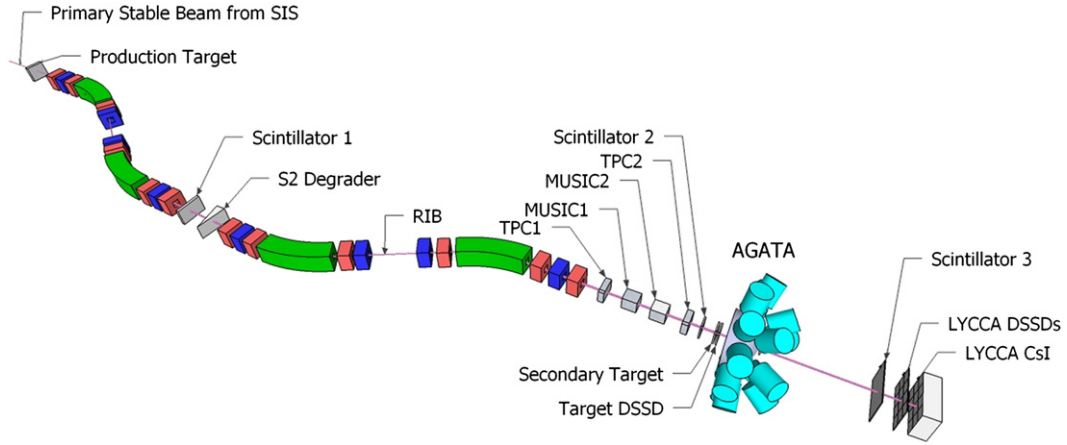
Fig. 1. Schematic representation of the PreSPEC set-up, showing the production target, FRS, beam-tracking detectors, AGATA and LYCCA. See text for details.
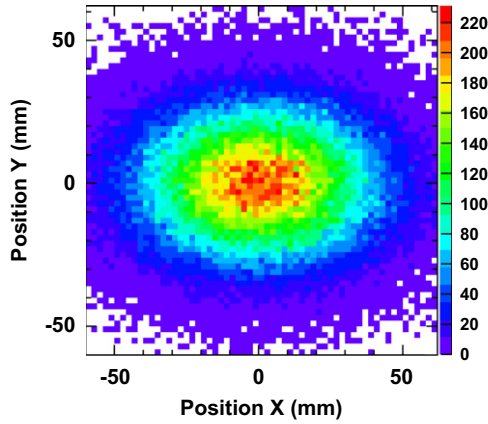

Fig. 2. Transversal spatial distribution of the RIB at the final FRS focal plane for an energy of $\sim 100\ \text{MeV}/u$.

200–500 mg/cm^2 can be used, which allow one to enhance the reaction rate, while keeping the angular straggling of the reaction products within reasonable values of 5–10 mrad. For many cases, such an enhancement on the reaction yield becomes of pivotal importance in order to access very exotic species, which are produced only in very small amounts (Fig. 3).

Because of the high reaction-product velocity β the measured γ-ray energy E_γ appears shifted with respect to the γ-quantum energy at rest $E_{\gamma,\circ}$. This effect can be corrected by applying the Doppler formula

$$E_{\gamma,\circ} = E_\gamma \frac{1 - \beta \cos \theta_\gamma}{\sqrt{1 - \beta^2}} \tag{1}$$

where θ_γ is the angle between the emitted γ-ray and the trajectory of the fragment in the laboratory frame. Thus, the accuracy with which the original γ-ray energy can be determined is dominated by the uncertainty in the determination of the angle θ_γ and the uncertainty in the measurement of the fragment velocity β at the moment of γ-ray emission. In theory, three positions are needed in order to derive the value of the angle θ_γ: the position of the reaction product at the time of de-excitation, the relative position downstream from the target, and the location of the first γ-ray hit in AGATA. In practice, however, the reaction-product position at de-excitation time can be measured only in an approximate way. Indeed, the two transversal (x,y)
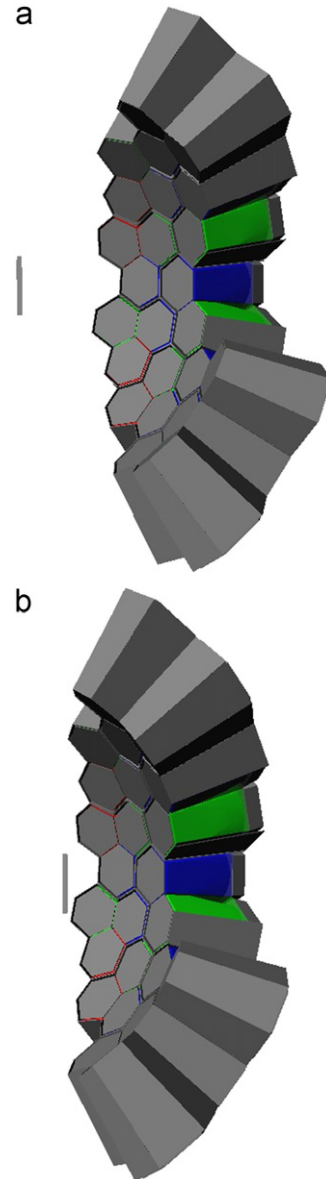

Fig. 3. Large (a) and short (b) AGATA configurations for optimizing resolution and efficiency, respectively.

coordinates of the fragment are determined, approximately, utilizing a double-sided silicon-strip detector (DSSD) placed close to the secondary target. At present, there is no technique to measure the z-position downstream of the reaction product at de-excitation time. For long half-life reaction products such uncertainty dominates the width of the Doppler corrected γ-ray spectrum (see Section 8). The trajectory of the reaction products downstream from the target is determined by using the Lund-York-Cologne CAlorimeter (LYCCA) [43]. A third plastic scintillator (Scintillator 3 in Fig. 1) enables the measurement of the velocity of the fragments or reaction products after the target β_{at}. Note that, in general, due to the energy loss in the target this quantity can be smaller than the velocity β at emission time, i.e. $\beta_{at} \leq \beta$, an effect which also has an impact in the attainable resolution (see Section 8). Finally, the 3D position sensitivity of AGATA, with an average FWHM $\simeq 4$ mm, provides the remaining information needed for the Doppler reconstruction of the γ-ray spectra. Further details about γ-ray spectroscopy experiments with RIB at GSI-FRS using the RISING array of EUROBALL cluster detectors can be found in Ref. [44].

3. Reference case for the conceptual design The AGATA double cluster detectors

A simplified, although representative, physics case has been simulated in order to evaluate several possible geometrical detector configurations and determine the array design best suited for experiments at GSI-FRS. The evaluation of the array performance is based on the attainable γ-ray photopeak efficiency, peak-to-total (P/T) ratio and energy resolution. The MC-code used for this purpose is described in Ref. [14], with minor modifications in order to include the specific spatial x,y-profile of the RIB at the final focus of the FRS (see Fig. 2). Also the event generator of Ref. [14] was used to emit γ-rays with an energy at rest of $E_{\gamma,\circ} = 1$ MeV emitted from a nucleus at a velocity of $\beta = 0.43$, equivalent to ~ 100 MeV/u commonly used for Coulomb excitation and particle knockout experiments at GSI-FRS.

In the conceptual design part of the present work, the effects related to the target thickness and half-life of the nuclear transition have been explicitly left aside. Such simplifications are convenient in order to tackle the problem in a systematic way. A negligible target thickness ensures no energy loss across the target, which implies a well defined velocity at de-excitation time ($\beta = 0.43$). Further, a prompt de-excitation (half-life $t_{1/2} = 0$) ensures a well defined emission angle θ_γ. The impact of the target details in the Doppler reconstructed spectra is reported later in detail in Section 8. The interplay between the value of the half-life and the target thickness is described in Section 9. These effects are expected to influence the performance of the array approximately in the same direction for all configurations and therefore, such assumptions are not expected to affect the conclusions of this section.

Another simplification concerns the γ-ray multiplicity, which has been assumed to be $M_\gamma = 1$ in all cases. Apart from the atomic background radiation, $M_\gamma = 1$ is a reasonable assumption for both Coulomb excitation experiments $M_\gamma^{Coulex} = 1-2$ and particle knockout reactions $M_\gamma^{Knockout} = 3-4$.

In order to set-up a versatile γ-ray detection system with a limited number of capsules available, it is foreseen that the target–array distance is adjusted according to the characteristics of each particular experiment. Thus, large (short) target–array distances can be set-up in order to optimize detection resolution (efficiency). This feature is reasonable when the array consists of a relatively small amount of 30–40 capsules. A larger number of detectors covering a solid angle of 2π or more would show

approximately a constant variation of the efficiency with the target–array distance. An intermediate distance can be also chosen in order to settle a compromise between efficiency and resolution. The so-called "large" distance corresponds to 23.5 cm, which represents the centre of the spherical shell defined by the front surface of the AGATA capsules. The "short" distance corresponds to a target–array distance of 8.5 cm.

Thus, the evaluation of each configuration is based on MC simulations for six different target–array distances of 23.5, 18.5, 15.5, 13.5, 11.5 and 8.5 cm, each case containing 5×10^5 events, which yields a negligible statistical uncertainty for all quoted results.

γ-ray tracking has been implemented for the reconstruction of the simulated events with the MGT-code [45]. MGT is used with both packing and smearing distances equal to 5 mm and intrinsic energy resolution for HPGe of 1.9 keV FWHM at $E_\gamma = 1.33$ MeV with a noise component of 1 keV. All the results presented in the following have been obtained by properly processing the raw simulated data with MGT.

The first aspect to be considered for the installation of AGATA at GSI is related to constraints arising from the size of the RIB at the final focal plane of the FRS. This also holds true for future implementations of AGATA for HISPEC experiments at FAIR-NUSTAR. On one hand, as shown in Fig. 2, because of the spatial spread of the RIB a beam-pipe with a diameter of $\gtrsim 80$ mm is required in order to avoid excessive interactions of the outgoing reaction products with the beam-pipe itself and other structural materials. Calculations of the ion-beam optics through the current design of the Super-FRS [46] indicate that the size of the beam at its final focal plane should be comparable to the one shown in Fig. 2. On the other hand, the geometrical design of AGATA aims to maximize the solid angle coverage, thus reducing to the minimum the size of the pentagonal holes [14]. The latter turn out to be sufficiently large for the beam output at LNL-INFN, but they are too small for the beam at GSI-FRS. The most straightforward solution would consist of removing two of the central triple clusters of the 1π AGATA configuration, and rotate slightly the array around the vertical axis, as it is shown in Fig. 4, top. Nevertheless, this option shows two strong drawbacks. First, it
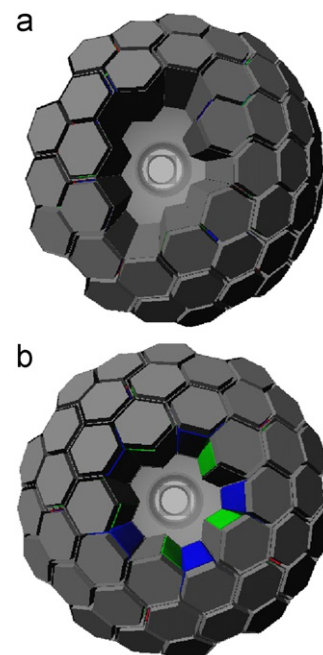

Fig. 4. (a) Shell geometry with 13 triple cluster detectors. (b) Hybrid shell geometry with 5 double- and 10-triple cluster detectors.

breaks the symmetry of the array, thus making difficult the distribution of the detectors and lending to an irregular growth and solid angle coverage of the array. Second, the irregular and relatively large insensitive area at forward angles is the most relevant region in terms of efficiency, due to the effect of the Lorentz boost.

One possibility to improve this situation consists of developing and implementing AGATA double cluster detectors (ADC detectors). The original conceptual design of AGATA [14] comprises an array of 180 irregular hexagons, using only three crystal shapes. The tree different geometries are assigned a letter and a colour: A – red, B – green and C – blue. Each AGATA triple cluster (ATC) is made from the three crystal shapes A, B and C sharing the same cryostat. The ADC detectors proposed here can be built from crystals of types B and C. This way, the removal of the five capsules of A type positioned around the pentagonal hole in the beam axis is done by using an inner ring of five ADC detectors. Thus, this AGATA implementation will be an hybrid configuration of ADC and ATC detectors, still in a 1π symmetric AGATA set-up (see Fig. 4b). This geometry optimizes the large solid angle coverage at forward angles, while leaving enough space for the RIB passing downstream towards LYCCA. Such approach yields a remarkable enhancement in performance when compared with any other possibility based only on ATC detectors. This is shown in Fig. 5, where the photopeak efficiency, energy resolution and P/T ratio are displayed as a function of the distance between the secondary target and the AGATA array. In this case, the geometry based on ATC detectors contains 13 of them, 39 capsules, as shown in Fig. 4, top. The new hybrid geometry is based on an outer ring of 10 ATCs, supplemented with an inner ring of 5 ADC detectors (40 capsules), as shown in Fig. 4b. Thus, an enhancement of up to 20% in efficiency can be achieved, whereas the resolution and P/T ratios remain essentially the same. The tracking efficiency of MGT typically varies between 60% and 80% for short (8.5 cm) and large (23.5 cm) target–array distances, respectively.

The evolution of the detection sensitivity with decreasing target–array distances reflects both, the effect of the larger solid-angle and the Lorentz boost at velocities of $\beta \sim 0.43$. When
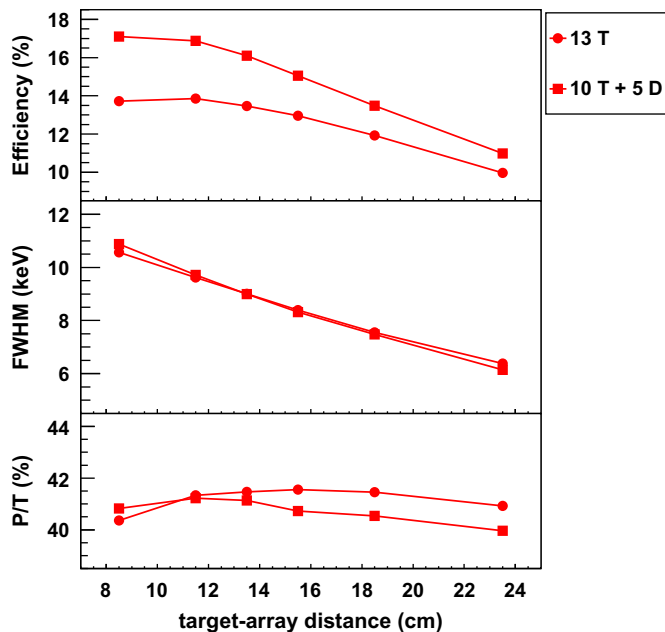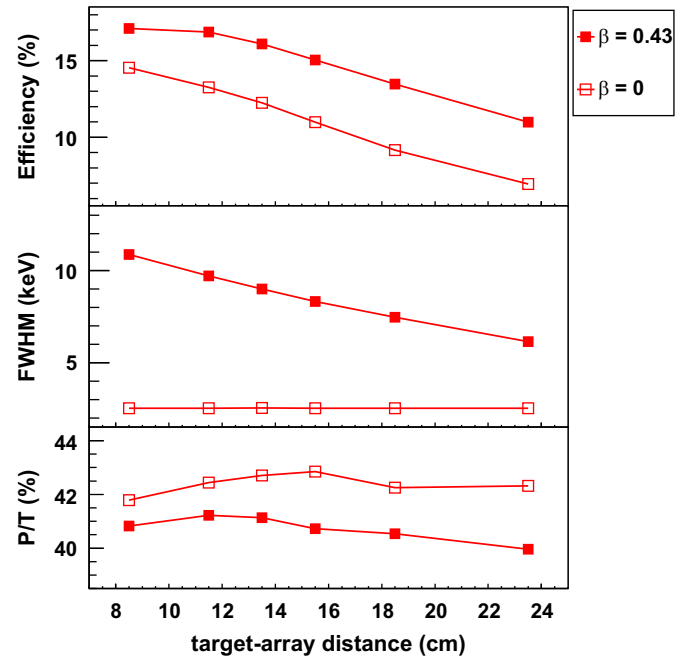

Fig. 6. Photopeak efficiency (top), resolution (middle), and P/T ratio (bottom) for the 10 ATC + 5 ADC AGATA configuration, at relativistic projectile energy $\beta = 0.43$ (solid symbols) and at rest (open symbols).

compared to an isotropic γ-ray emission distribution, the Lorentz boost represents an advantage in terms of detection efficiency particularly for large target–array distances. This effect is illustrated in the top panel of Fig. 6, where the performance of the 10 T+5 D geometry is shown for a projectile having a velocity of $\beta = 0.43$ and at rest $\beta = 0$.

Other configurations investigated were based on compact cylindrical geometries, where the ATC detectors were separated from each other, and arranged around the target chamber for maximizing the solid angle coverage. This approach had the disadvantage that γ-ray tracking could be only applied within each ATC detector, thus reducing the overall performance of the array in terms of efficiency and P/T ratio, and notably limiting the scalability of the array on a long term basis. This issue of scalability is explored further in Section 4.

In summary, the MC performance figures indicate that an hybrid shell-geometry, based on an inner ring of 5 ADCs, and an outer ring of ATC detectors (as many as available) represents the best approach for nuclear structure studies using relativistic RIBs at the GSI-FRS facility and at the future FAIR-NUSTAR site.

4. Performance of the hybrid shell geometry

The non-proportionality of the efficiency with the number of capsules in the array, due to the tracking concept, makes it worth quantifying the performance of the hybrid array as a function of the number of ADC and ATC detectors available. Using the reference case described in the above section the expected performance in terms of γ-ray photopeak efficiency, resolution and P/T-ratio is shown in Table 1 (Table 2) for 5 ADCs (ATCs) and a variable number of ATCs (ADCs). For the sake of clarity, these values are shown in Fig. 7 only for configurations consisting of n ATC and 5 ADC detectors (n T+5 D), with n being a representative number of ATC detectors between 0 and 10. Fig. 8 shows the performance for 5 ATCs and a variable number of ADCs (5 T+n D), with n from 0 up to 5 ADC detectors. In the latter figure, also the combination 0 T+5 D is shown. It is worth emphasizing the

Fig. 5. Photopeak efficiency (top), resolution (middle), and P/T ratio (bottom) for two AGATA configurations: 13 triple clusters (circles) shown in Fig. 4, top, and 5 double-plus 10 triple-cluster detectors (squares) as shown in Fig. 4b.

Table 1
Performance of the AGATA array as a function of the number of ATC detectors, assuming always an inner ring of 5 ADCs. For each configuration indicated on the left-hand side of the table, the three rows represent the efficiency, resolution and *P/T* ratio, respectively.

No. of		Distance target–array (cm)						
ATC	ADC	23.5	18.5	15.5	13.5	11.5	8.5	
10	5	11.0	13.5	15.1	16.1	16.9	17.1	ε_γ (%)
		6.1	7.5	8.3	9.0	9.7	10.9	FWHM (keV)
		40.0	40.5	40.7	41.1	41.2	40.8	P/T (%)
9	5	10.0	12.4	13.9	14.9	15.6	16.0	ε_γ (%)
		6.1	7.4	8.3	8.9	9.7	10.8	FWHM (keV)
		39.6	40.0	40.4	40.5	40.4	40.1	P/T (%)
8	5	9.0	11.2	12.7	13.5	14.1	14.7	ε_γ (%)
		6.0	7.3	8.3	8.9	9.7	10.9	FWHM (keV)
		39.1	39.7	40.0	39.7	39.7	39.2	P/T (%)
7	5	8.0	10.0	11.4	12.3	13.1	13.8	ε_γ (%)
		5.9	7.3	8.2	8.9	9.8	11.0	FWHM (keV)
		38.3	38.5	39.0	38.9	39.1	38.8	P/T (%)
6	5	6.9	8.8	10.1	10.8	11.6	12.4	ε_γ (%)
		5.8	7.2	8.1	8.8	9.7	11.1	FWHM (keV)
		36.9	37.6	37.8	37.6	38.0	37.6	P/T (%)
5	5	6.0	7.6	8.9	9.7	10.4	11.3	ε_γ (%)
		5.7	7.1	8.0	8.8	9.7	11.1	FWHM (keV)
		35.8	36.3	36.7	36.9	36.7	36.5	P/T (%)
4	5	5.0	6.4	7.6	8.3	9.1	10.0	ε_γ (%)
		5.5	6.9	7.9	8.8	9.6	11.1	FWHM (keV)
		34.6	35.1	35.3	35.3	35.5	35.2	P/T (%)
3	5	4.1	5.4	6.4	7.1	7.9	9.0	ε_γ (%)
		5.3	6.8	7.8	8.7	9.6	11.3	FWHM (keV)
		32.7	33.0	33.5	33.7	33.8	33.8	P/T (%)
2	5	3.2	4.2	5.2	5.8	6.7	7.9	ε_γ (%)
		4.9	6.4	7.6	8.5	9.5	11.5	FWHM (keV)
		31.5	31.5	32.2	32.0	32.3	32.9	P/T (%)
1	5	2.7	3.6	4.4	5.0	5.7	6.8	ε_γ (%)
		4.9	6.3	7.6	8.6	9.6	11.4	FWHM (keV)
		31.2	31.2	31.6	31.7	31.7	31.8	P/T (%)
0	5	2.0	2.7	3.3	3.8	4.3	5.2	ε_γ (%)
		4.8	6.4	7.5	8.4	9.7	11.4	FWHM (keV)
		29.6	29.9	30.3	30.0	30.4	30.4	P/T (%)

Table 2
Performance of the AGATA array for five ATCs and a variable number of ADC detectors. For each configuration indicated on the left-hand side of the table, the three rows represent the efficiency, resolution and *P/T* ratio, respectively.

| No. of		Distance target–array (cm)						
ATC	ADC	23.5	18.5	15.5	13.5	11.5	8.5	
5	4	5.5	7.0	7.9	8.5	9.1	9.7	ε_γ (%)
		5.9	7.4	8.4	9.3	10.2	12.1	FWHM (keV)
		35.7	36.2	36.5	36.2	36.3	36.1	P/T (%)
5	3	5.4	6.6	7.3	7.8	8.4	8.6	ε_γ (%)
		6.1	7.5	8.6	9.4	10.3	11.8	FWHM (keV)
		37.8	37.7	37.6	37.8	38.1	37.5	P/T (%)
5	2	5.0	6.0	6.7	7.1	7.3	7.4	ε_γ (%)
		6.3	7.7	8.7	9.4	10.2	11.8	FWHM (keV)
		38.6	38.9	39.4	39.2	39.3	39.1	P/T (%)
5	1	4.5	5.4	5.9	6.1	6.2	6.1	ε_γ (%)
		6.5	7.8	8.8	9.6	10.4	11.4	FWHM (keV)
		38.5	39.1	39.5	39.1	39.0	38.7	P/T (%)
5	0	4.0	4.7	5.0	5.1	5.1	4.8	ε_γ (%)
		6.9	8.3	9.1	9.6	10.2	10.9	FWHM (keV)
		38.3	38.7	38.9	38.9	38.2	37.8	P/T (%)
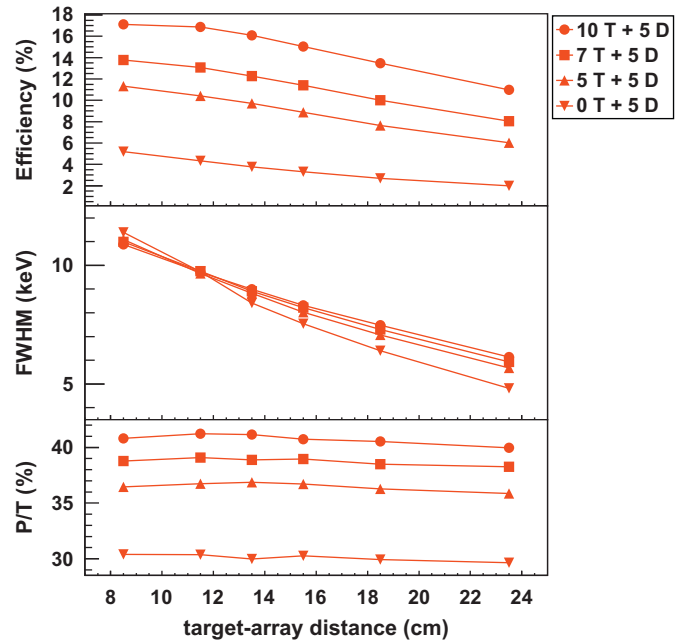
Fig. 7. Reference case. Efficiency (top), resolution (middle) and *P/T* ratio (bottom) as a function of the number of ATC detectors in the set-up. The number of ADC detectors is always 5.
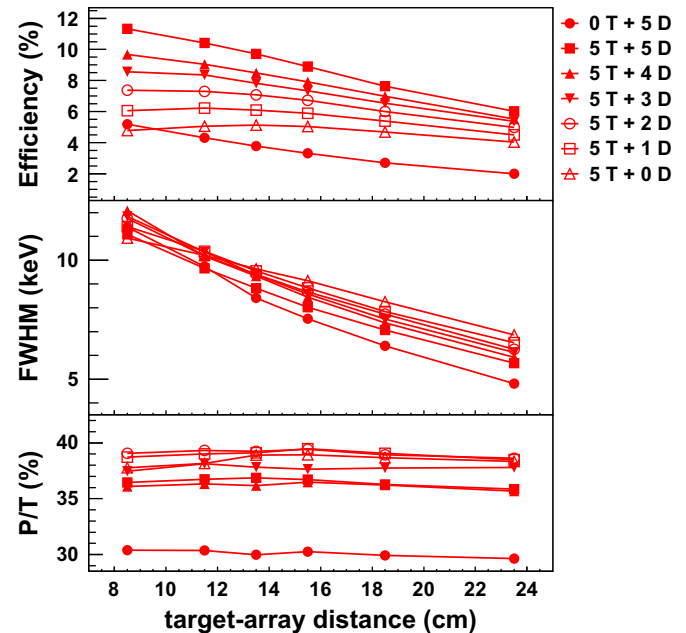

Fig. 8. Reference case. Efficiency (top), resolution (middle) and *P/T* ratio (bottom) as a function of the number of ADC detectors (#D) in the set-up. All configurations comprise 5 ATCs.

similarity in the performance between the 0 T+5 D and the 5 T+0 D cases at short target-array distances. This illustrates, once more, the relevance of developing ADC detectors for experiments at GSI. Indeed, 10 capsules arranged in a ring of 5 ADCs show at short target-array distances, the same performance as 15 capsules arranged in a half-ring of 5 ATCs detectors. In this respect, it is also important to remark the non-linear dependence of the detection efficiency on the number of capsules, as a consequence of γ-ray tracking. For example, at 11.5 cm, the 5 T+0 D case corresponds to an intrinsic photopeak efficiency of 0.34% per capsule. On the other hand, the 5 T+5 D configuration shows an

efficiency of 0.45% per capsule, which indicates a relative enhancement of the detection efficiency per capsule of 32%.

For the first experiments with AGATA at GSI, it is expected that at least 5 ATCs and 5 ADCs are available. Therefore, for nuclear transitions of 1 MeV emitting at $\beta = 0.43$, photopeak efficiencies in the range of 6 to 11% and energy resolutions of 6 to 11 keV should be attainable (depending on the distance target–array) with a P/T ratio of about 36%. The asymmetry in the spatial distribution of the beam, which is larger in the dispersive plane x than in the vertical direction y, has been found to have a negligible impact in the efficiency of the 5 D+5 T configuration. When the 5 ATCs are placed together the efficiency does not depend on their position around the inner ring of ADCs. Furthermore, it is worth noting that the outer ring of ATCs is actually composed of two sub-rings. One of them subtends slightly lower forward angles (Fig. 9b) than the other one (Fig. 9c). Thus, one might think of distributing the five ATCs semi-consecutively, as it is shown in the two bottom configurations displayed in Fig. 9. This option, however, shows an slightly reduced efficiency. The efficiency of 6% obtained with the geometry shown in Fig. 9a for the nominal distance of 23.5 cm, is reduced to 5.9% and 5.8% for the configurations shown in Fig. 9b and c, respectively. This can be ascribed to the larger open surface exposed by the ATCs and the corresponding decrease in the performance of the tracking algorithm.

The efficiency will increase gradually further when additional ATCs are installed in the set-up, thus reaching for a configuration with 5 ADC and 10 ATC detectors up to 11–17% photopeak efficiency, 6–11 keV FWHM energy resolution and $\sim 40\%$ P/T-ratio.
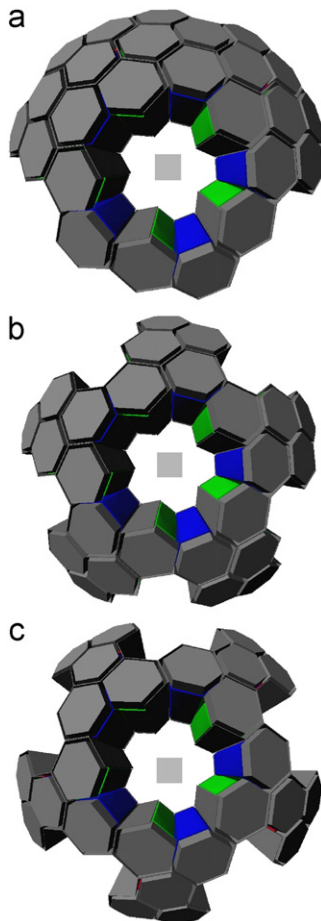
It is worth noting that, at least in terms of efficiency, there is an optimal target–array distance. However, the latter depends on the number and type of cluster detectors available. Thus, for a relatively small amount of clusters, there is a substantial enhancement in the efficiency when going from an intermediate distance as 11.5 cm to the shortest one of 8.5 cm, e.g. 9% enhancement for 5 ATC + 5 ADC detectors. However, such improvement is of only 1% for the 10 ATC + 5 ADC configuration.

The chosen γ-ray energy of $E_{\gamma,\circ} = 1$ MeV corresponds only to an average representative value, which is close to many experiments of interest for nuclear structure. Values for another γ-ray energies are reported in Section 5.

5. Dependence of the performance on the γ-ray energy

The complex dependency of the detection efficiency on the γ-ray transition energy using relativistic RIBs requires a MC simulation study. On one hand, the Lorentz boost concentrates a large amount of γ-quanta in the forward direction, thus enhancing the detection probability for small values of the angle θ_γ, mostly in the region covered by the ADC detectors. But on the other hand, this effect is counter-balanced to some extent by the Doppler shift in energy, which increases the γ-ray energy at the same forward angles, thus reducing the detection efficiency correspondingly. In order to quantify the impact of these effects in the performance of the tracking array, MC simulated values for efficiency, resolution and P/T-ratio, are tabulated and displayed in this section for a range of γ-ray energies from 500 keV up to 5 MeV. Results are reported for three reference hybrid-shell AGATA geometries, namely 10 ATC+5 ADC (Fig. 10, Table 3), 7 ATC+5 ADC (Fig. 11, Table 4) and 5 ATC+5 ADC (Fig. 12, Table 5).

6. Angular distribution of the efficiency

Angular distribution measurements of γ-rays emitted by oriented nuclei have been a fundamental tool to investigate their

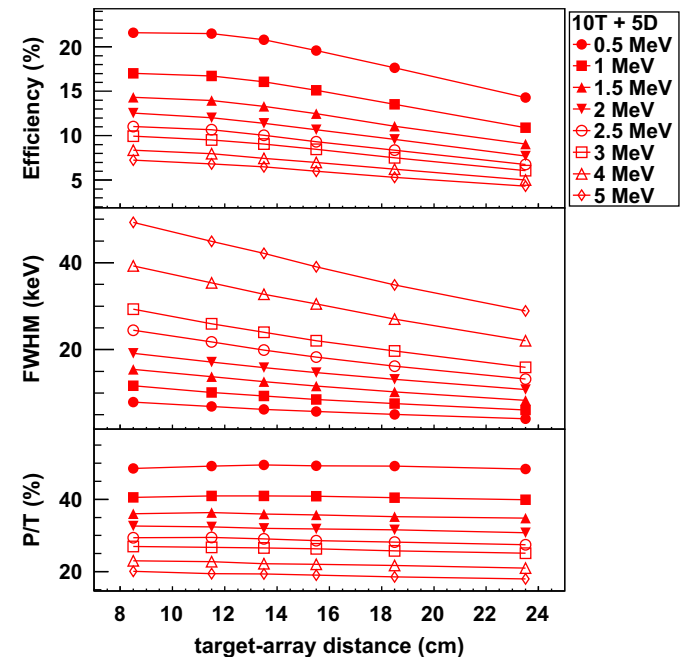**Fig. 9.** Possible configurations of AGATA with 5 D+5 T, ordered from top to bottom by decreasing efficiency.

Fig. 10. Photopeak efficiency (top), resolution (middle) and P/T ratio (bottom) for 10 ATC + 5 ADC detectors. Each curve corresponds to one γ-ray energy (see label). In all cases $\beta = 0.43$.

Table 3
10ATC+5ADC AGATA configuration, efficiency and energy resolution values as a function of the γ-ray energy at rest $E_{\gamma,\circ}$ and $\beta = 0.43$.

$E_{\gamma,\circ}$ (MeV)	Distance target–array (cm)						
	23.5	18.5	15.5	13.5	11.5	8.5	
0.5	14.3	17.6	19.6	20.8	21.5	21.6	ε_γ (%)
	4.1	5.0	5.7	6.2	6.9	7.9	FWHM (keV)
	48.4	49.2	49.2	49.5	49.2	48.6	P/T (%)
1	10.9	13.5	15.1	16.1	16.7	17.0	ε_γ (%)
	6.1	7.5	8.5	9.3	10.1	11.7	FWHM (keV)
	39.9	40.5	40.9	40.9	41.0	40.6	P/T (%)
1.5	9.1	11.1	12.5	13.3	14.0	14.3	ε_γ (%)
	8.3	10.3	11.6	12.6	13.8	15.4	FWHM (keV)
	34.8	35.2	35.7	35.9	36.3	36.0	P/T (%)
2	7.7	9.6	10.7	11.4	12.0	12.6	ε_γ (%)
	10.8	13.2	14.7	15.9	17.1	19.1	FWHM (keV)
	30.8	31.5	31.8	31.9	32.4	32.6	P/T (%)
2.5	6.8	8.4	9.3	10.1	10.7	11.0	ε_γ (%)
	13.2	16.2	18.3	19.9	21.7	24.5	FWHM (keV)
	27.4	28.2	28.5	29.0	29.5	29.4	P/T (%)
3	6.1	7.5	8.5	9.1	9.5	9.9	ε_γ (%)
	15.9	19.7	22.0	24.0	26.0	29.3	FWHM (keV)
	25.1	25.7	26.3	26.6	26.7	26.9	P/T (%)
3.5	5.5	6.8	7.6	8.2	8.6	9.1	ε_γ (%)
	18.9	23.2	26.0	28.4	30.6	34.4	FWHM (keV)
	22.8	23.4	23.9	24.3	24.4	24.8	P/T (%)
4	5.0	6.2	7.0	7.5	8.0	8.4	ε_γ (%)
	22.0	27.0	30.5	32.8	35.3	39.3	FWHM (keV)
	21.0	21.7	22.0	22.2	22.8	23.0	P/T (%)
4.5	4.6	5.7	6.5	6.9	7.3	7.7	ε_γ (%)
	25.4	31.3	34.9	37.3	39.8	44.2	FWHM (keV)
	19.2	20.0	20.5	20.7	21.0	21.4	P/T (%)
5	4.3	5.3	6.0	6.5	6.8	7.2	ε_γ (%)
	28.9	34.9	39.0	42.2	44.9	49.3	FWHM (keV)
	18.0	18.6	19.0	19.3	19.5	20.0	P/T (%)

Table 4
7ATC+5ADC AGATA configuration, efficiency, energy resolution and P/T-ratio values as a function of the γ-ray energy at rest $E_{\gamma,\circ}$ and $\beta = 0.43$.

| $E_{\gamma,\circ}$ (MeV)	Distance target–array (cm)						
	23.5	18.5	15.5	13.5	11.5	8.5	
0.5	10.5	13.2	15.0	16.1	17.0	17.7	ε_γ (%)
	3.9	4.9	5.6	6.1	6.8	8.0	FWHM (keV)
	46.3	47.0	47.6	47.5	47.2	46.7	P/T (%)
1	8.0	10.1	11.4	12.3	13.0	13.7	ε_γ (%)
	5.9	7.3	8.4	9.2	10.1	11.8	FWHM (keV)
	38.0	38.7	38.8	39.1	38.9	38.7	P/T (%)
1.5	6.6	8.2	9.4	10.1	10.7	11.4	ε_γ (%)
	8.1	10.0	11.5	12.5	13.7	16.0	FWHM (keV)
	32.9	33.4	33.8	33.9	34.0	34.0	P/T (%)
2	5.6	7.0	8.0	8.6	9.2	9.8	ε_γ (%)
	10.3	12.8	14.7	16.1	17.7	20.3	FWHM (keV)
	29.0	29.5	29.9	30.1	30.3	30.4	P/T (%)
2.5	5.0	6.1	6.9	7.6	8.0	8.6	ε_γ (%)
	12.7	15.7	18.2	20.2	21.7	25.0	FWHM (keV)
	26.1	26.5	26.6	27.0	27.1	27.3	P/T (%)
3	4.3	5.4	6.2	6.6	7.2	7.7	ε_γ (%)
	15.4	19.2	21.9	23.9	26.0	30.0	FWHM (keV)
	23.2	23.8	24.2	24.1	24.8	24.8	P/T (%)
3.5	3.9	4.9	5.7	6.0	6.5	7.0	ε_γ (%)
	18.1	22.9	25.8	28.1	30.9	35.1	FWHM (keV)
	21.2	21.5	22.2	22.3	22.5	22.8	P/T (%)
4	3.5	4.4	5.1	5.5	5.9	6.4	ε_γ (%)
	21.3	26.8	29.9	32.9	35.9	40.1	FWHM (keV)
	19.2	19.8	20.2	20.4	20.7	20.9	P/T (%)
4.5	3.3	4.1	4.7	5.0	5.4	5.8	ε_γ (%)
	24.8	30.8	34.6	37.4	40.5	44.9	FWHM (keV)
	17.7	18.1	18.6	18.6	19.0	19.2	P/T (%)
5	3.0	3.8	4.3	4.7	5.1	5.5	ε_γ (%)
	28.0	34.8	39.5	42.2	45.4	50.3	FWHM (keV)
	16.4	16.8	17.0	17.5	17.8	18.0	P/T (%)
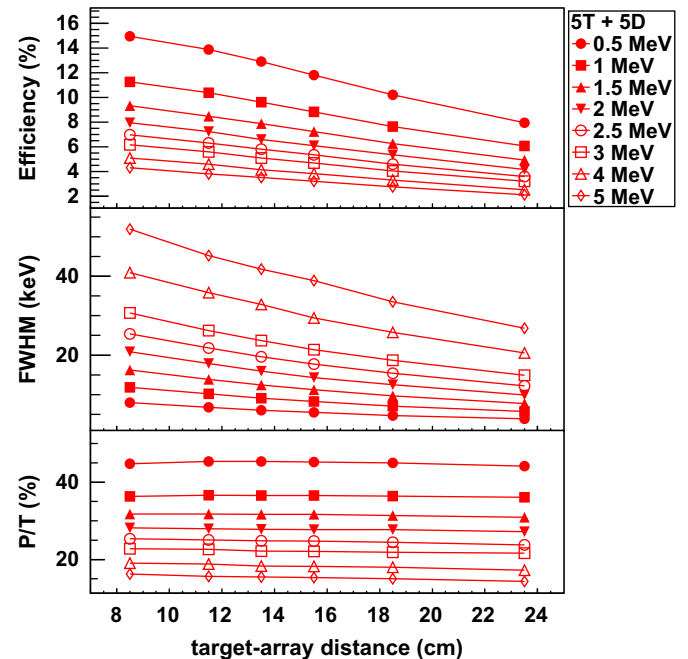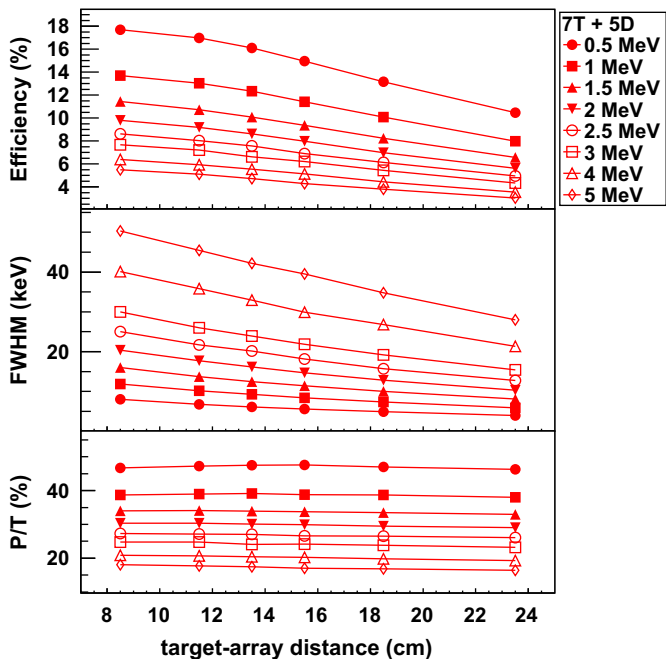
Fig. 11. Photopeak efficiency (top), resolution (middle) and P/T ratio (bottom) for 7 ATC + 5 ADC detectors. Each curve corresponds to one γ-ray energy (see figure label). In all cases $\beta = 0.43$.

Fig. 12. Photopeak efficiency (top), resolution (middle) and P/T ratio (bottom) for 5 ATC+5 ADC detectors. Each curve corresponds to one γ-ray energy (see figure label). In all cases $\beta = 0.43$.

Table 5
$\underline{5\text{ATC}+5\text{ADC}}$ AGATA configuration, efficiency and resolution values as a function of the γ-ray energy at rest $E_{\gamma,\circ}$ and $\beta = 0.43$.

$E_{\gamma,\circ}$ (MeV)	Distance target–array (cm)						
	23.5	18.5	15.5	13.5	11.5	8.5	
0.5	8.0	10.2	11.8	12.9	13.9	14.9	ε_γ (%)
	3.8	4.7	5.5	6.0	6.8	8.0	FWHM (keV)
	44.1	45.0	45.2	45.4	45.4	44.8	P/T (%)
1	6.1	7.6	8.8	9.6	10.4	11.2	ε_γ (%)
	5.7	7.1	8.2	9.1	10.2	11.8	FWHM (keV)
	36.1	36.4	36.5	36.6	36.6	36.4	P/T (%)
1.5	4.9	6.3	7.2	7.9	8.5	9.3	ε_γ (%)
	7.7	9.7	11.3	12.4	13.8	16.2	FWHM (keV)
	30.9	31.4	31.7	31.7	31.7	31.8	P/T (%)
2	4.2	5.4	6.1	6.6	7.2	8.0	ε_γ (%)
	9.9	12.5	14.3	15.9	17.9	20.8	FWHM (keV)
	27.2	27.8	27.7	27.8	28.0	28.2	P/T (%)
2.5	3.6	4.6	5.4	5.8	6.3	7.0	ε_γ (%)
	12.2	15.4	17.7	19.6	21.8	25.4	FWHM (keV)
	23.7	24.4	24.8	24.8	25.0	25.3	P/T (%)
3	3.2	4.1	4.7	5.1	5.6	6.2	ε_γ (%)
	14.9	18.7	21.4	23.7	26.2	30.7	FWHM (keV)
	21.7	21.8	22.1	22.1	22.6	22.8	P/T (%)
3.5	2.9	3.7	4.2	4.6	5.0	5.6	ε_γ (%)
	17.7	21.8	25.5	28.2	30.6	35.5	FWHM (keV)
	19.6	19.8	20.1	20.2	20.3	20.6	P/T (%)
4	2.5	3.3	3.8	4.2	4.6	5.1	ε_γ (%)
	20.5	25.8	29.4	32.9	35.9	40.9	FWHM (keV)
	17.2	18.0	18.2	18.3	18.8	19.0	P/T (%)
4.5	2.3	3.0	3.5	3.8	4.2	4.7	ε_γ (%)
	23.8	30.1	33.7	37.9	41.0	46.3	FWHM (keV)
	15.7	16.4	16.5	16.7	17.2	17.6	P/T (%)
5	2.1	2.8	3.2	3.5	3.8	4.3	ε_γ (%)
	26.8	33.5	38.9	41.8	45.3	51.9	FWHM (keV)
	14.4	15.0	15.3	15.5	15.7	16.2	P/T (%)

Fig. 13. Efficiency as a function of the γ-ray detection angle θ_γ for $E_{\gamma,\circ} = 1$ MeV emitted at $\beta = 0.43$. (a) A simulation with 10 ATC and 5 ADC detectors and (b) 5 ATC and 5 ADC detectors.

These two contributions are most visible in the "short" distance configuration ($d = 8.5$ cm), where two maxima can be observed at $\sim 55°$ and at $\sim 75°$ (see Fig. 13a). Comparing the angular distribution of 10 T+5 D (Fig. 13a) against that of 5 T+5 D (Fig. 13b), one can indeed observe a reduction in the efficiency due to the lowering of the second maximum, i.e. the contribution of the outer ring of only five ATC detectors.

7. Impact of passive materials

At the final stage of the GSI-FRS the main source of γ-ray background is due to the slowing-down of ions and light-charged particles, flying through layers of materials such as the energy-degrader, the secondary target, the tracking detectors and other structural materials like the beam-pipe and holding structures. Experimental γ-ray spectra with such background measured with RISING have been shown in the previous publications [41,49]. A description of this background at the lower beam-energies used in decay-spectroscopy experiments is reported in Ref. [50]. In order to suppress effectively the contribution of the bremsstrahlung's radiation to this background, a lead layer was installed around the EUROBALL cluster detectors in the RISING campaigns. In a similar way, it might be convenient to put a lead shielding around the reaction chamber to reduce the background in AGATA. This is a possibility which will be investigated during the commissioning of AGATA at GSI, because due to the complexity of this background, simulations are unlikely to predict it accurately enough. Nevertheless, the effect of such a lead layer with different thicknesses around the target chamber to shield the AGATA detectors can be simulated and is illustrated in Fig. 14, which shows the result of a MC simulation for $E_{\gamma,\circ} = 1$ MeV emitted at $\beta = 0.43$. Three configurations have been considered

multipolarity and electromagnetic character (see e.g. [47]). In addition, the angular distribution of the prompt γ-rays emitted after the Coulomb excitation allows one to distinguish between the electromagnetic and the nuclear contributions to the excited states. Such studies were performed in the past at GSI using an array of EUROBALL cluster detectors [48,41]. The high granularity of AGATA in conjunction with the large angular range represents a substantial advantage in order to study angular distributions in detail. The broad angular coverage arises not only from the number of germanium crystals available, but also from the possibility to shift the secondary target downstream by 15 cm. This is illustrated in Fig. 13, where the γ-ray efficiency for $E_{\gamma,\circ} = 1$ MeV emitted from a nucleus at $\beta = 0.43$ is displayed as a function of the angle θ_γ in intervals of $\Delta\theta_\gamma = \pm 5°$. Note that the integral of the curves seen in Fig. 13 will return the matching efficiency values presented in the tables and figures of the preceding section.

Thus, in the AGATA configuration of 10 ATC and 5 ADC detectors, angles between $15°$ and $90°$ can be covered with angular efficiencies larger than 1% over $\Delta\theta = 10°$. Note that at relativistic beam energies ($\beta \sim 0.43$), the largest differences between the electromagnetic and the nuclear interactions are obtained at $\theta_\gamma \simeq 25°$ and at $\theta_\gamma \simeq 60°$. At these angles, the proposed geometry allows one to achieve efficiencies of more than 2.5% over an interval of $\Delta\theta_\gamma = \pm 5°$.

The angular distribution of the first interaction reflects the contribution in efficiency of both, the inner ring of ADC and the outer ring of ATC detectors, even if they are not independent.
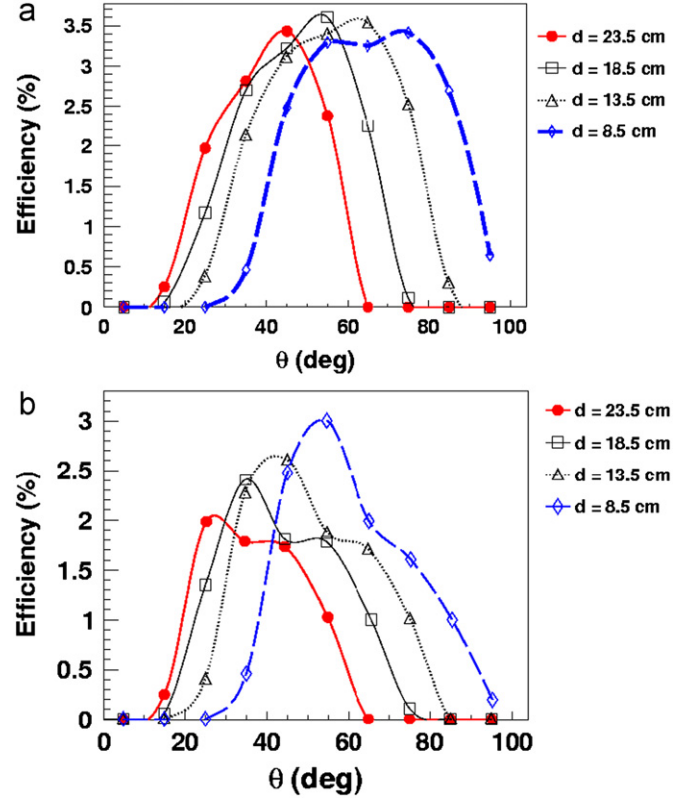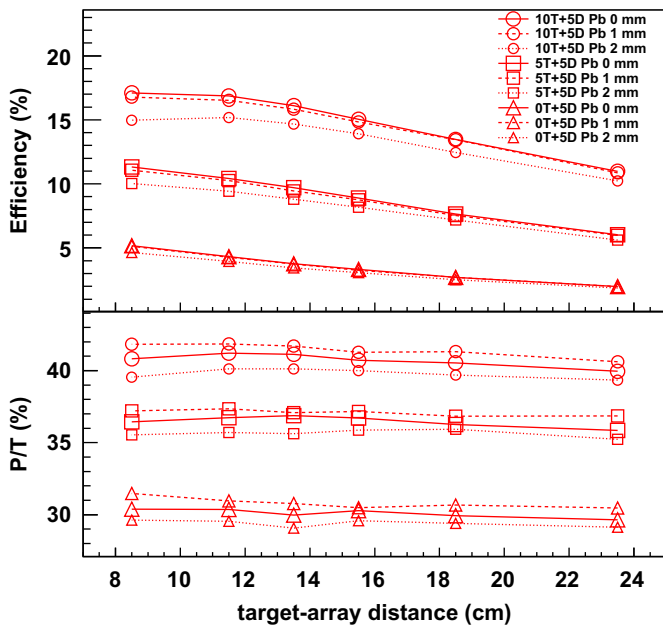
Fig. 14. Biggest symbols represent values without lead absorber, the empty symbols with decreasing size show the deterioration of the efficiency (top panel) and P/T ratio (bottom) due to a layer of lead in-front of the detectors. See legend for proper interpretation of the absorber thickness. MC simulation performed for $E_{\gamma,\circ} = 1$ MeV emitted at $\beta = 0.43$.

in the simulation, (i) 10 ATC+5 ADC, (ii) 5 ATC+5 ADC and (iii) 5 ADC detectors. Indeed, the impact of a lead layer, both in the efficiency and in the P/T ratio, becomes larger for the ATCs than for the ADCs, and also for the short target–array distance of 8.5 cm than for the nominal distance (see Fig. 14). This reflects the energy shift due to the large Doppler effect at relativistic velocities, which yields smaller energies (larger absorption) at the larger angles subtended by the ATCs, when compared to the small angles (larger energy) subtended by the ADCs. The resolution (not shown in Fig. 14) remains practically unaffected.

8. Interplay between target thickness and half-life of the nuclear transition

The impact of the target characteristics and the excited state lifetime on the shape of Doppler corrected γ-ray spectra has been thoroughly investigated in Ref. [51] for in-beam γ-ray experiments at relativistic energies using the RISING array. A similar study for AGATA is presented in this section.

The convoluted effect of the excited state lifetime and the energy loss across the target thickness is due to the fact that the target is a passive element, and therefore, both the reaction-product velocity and position at de-excitation time, in general, remain unknown. In practice, only the measurement of the reaction-product velocity after the target, β_{at}, becomes feasible. If the lifetime is sufficiently short, so that the average de-excitation path is shorter than the target thickness, most of the transitions still occur inside the target, where no kinematics information is available, i.e. the velocity at de-excitation time β is unknown and larger than the velocity measured after the target β_{at} with LYCCA (see Section 2). On the other hand, nuclei with relatively long half-lives de-excite predominantly beyond the secondary target, and the velocity at de-excitation time β coincides with the velocity measured after the target β_{at}. In the latter case, the Doppler correction becomes precise in terms of velocity.

However, the position downstream along the beam axis z at de-excitation time remains still unknown and the true γ-ray emission angle θ_γ is larger than the one commonly assumed, which corresponds to de-excitations at the centre of the target. This feature introduces an exponential tail towards low energy in the Doppler corrected photopeak, which is larger the longer is the lifetime. In general, the shape of the Doppler reconstructed spectrum reflects the contribution of these two effects, whose relative influence depends sensitively on the beam and target characteristics, as well as on the precise value of the transition lifetime. In order to illustrate this, a series of MC simulations have been carried out, with an AGATA configuration consisting of 10 ATC and 5 ADC, with secondary targets of Au and Be, with thicknesses of 250 and 500 mg/cm² and target–array distances of 8.5 and 23.5 cm. These are the most extreme scenarios in terms of optimizing detection efficiency, resolution or reaction yield (see Sections 2 and 3). For each case, transition half-lives between 0 ps and 100 ps have been simulated.

The physics case corresponds to a medium-heavy nucleus ($Z=29$, $A=75$) impinging at a velocity of $\beta = 0.43$ in the secondary target, and undergoing a one-proton knockout reaction. The spatial distribution along the beam direction z assumed for the generation of the primary events in the simulation corresponds to a constant excitation cross-section across the path of the nucleus through the target. The event generator is the one described in Ref. [51] with only minor updates to interface with the standard AGATA-code [14]. A transition energy of $E_{\gamma,\circ} = 1$ MeV is assumed in all cases.

8.1. Light secondary target

The Doppler corrected spectra for beryllium targets of 250 and 500 mg/cm² are shown in Figs. 15 and 16, respectively. Also the spectrum corresponding to an ideally thin target is shown in those figures for comparison.
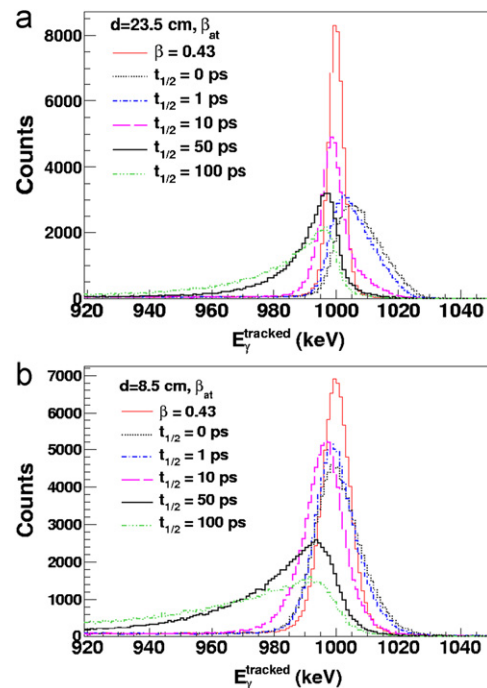

Fig. 15. Effect of the lifetime and the energy loss across a 250 mg/cm² thick beryllium target. The velocity after the target has been taken for the Doppler reconstruction. Simulation for target–array distance of 23.5 cm (a) and 8.5 cm (b). The thin-solid line (labelled as $\beta = 0.43$) corresponds to an ideal target of negligible thickness and prompt de-excitations ($t_{1/2} = 0$ ps). See text for details.
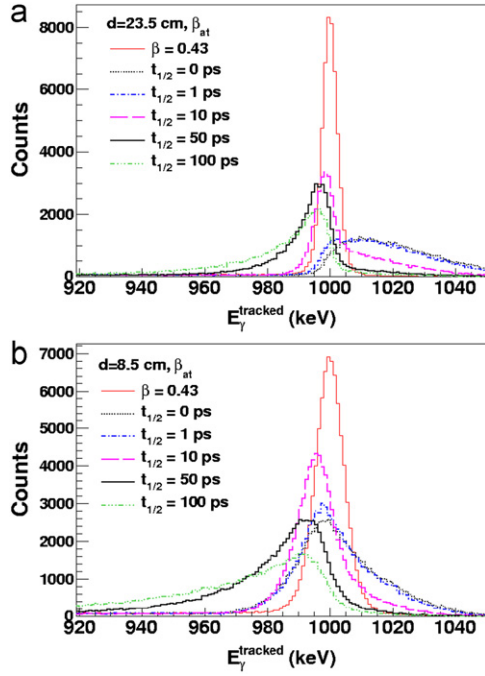
Fig. 16. Same as Fig. 15, but for a 500 mg/cm^2 thick Be-target.

Table 6
Estimated γ-ray energy resolution simulated for de-excitations from a reaction on a beryllium target for several assumptions of the target thickness and the half-life of the transition.

$t_{1/2}$ (ps)	RESOLUTION FWHM [FWTM] (keV)			
	250 mg/cm^2		500 mg/cm^2	
	$d=23.5$ cm	$d=8.5$ cm	$d=23.5$ cm	$d=8.5$ cm
0	17 [32]	17 [34]	37 [61]	23 [54]
1	16 [30]	16 [31]	35 [62]	20 [56]
10	8 [23]	15 [32]	8 [36]	14 [38]
50	13 [36]	25 [76]	12 [32]	24 [67]
100	17 [60]	41 [150]	16 [50]	34 [120]

For the Doppler correction the (measurable) reaction-product velocity after the target, β_{at}, has been considered and the γ-ray emission angle in the laboratory system, θ_γ, has been calculated assuming a de-excitation position along the beam axis at $z=0$ cm, i.e., at the centre of the target.

The width of the photopeak reconstructed via MGT is reported in Table 6. Note that in some cases the shape of the reconstructed photopeak is rather asymmetric, and in those situations the value of the FWHM is not very representative. Therefore, the value of the full width at 10th maximum FWTM is also given in Table 6.

As previously mentioned, the main deviations from the ideal target case arise from two experimental effects. On one hand, for transitions where $t_{1/2}$ is small the width of the reconstructed peak is dominated by energy loss effects inside the target and the corresponding uncertainty on β at de-excitation time. As shown for the 500 mg/cm^2 target in Fig. 16a, this effect is particularly prominent for half-lives around $t_{1/2} \lesssim 1$ ps. The tail towards high γ-ray energy is due to the assumption $\beta \sim \beta_{at}$. Actually, the fact that $\beta > \beta_{at}$ introduces a shift in the value of the Doppler reconstructed energy towards high energy (see Eq. (1)). On the other hand, for transitions with large half-lives ($t_{1/2} \gtrsim 50$ ps) the width of the reconstructed peak is dominated by the uncertainty on the de-excitation position z along the beam axis. Assuming a de-excitation at $z=0$ leads to an emission angle θ_γ smaller than

the true angle downstream $z>0$, an effect that goes in the opposite direction than the aforementioned $\beta \sim \beta_{at}$ approximation, shifting the value of the reconstructed energy towards low energy. One can quantify the strength of these two effects by means of the ratio FWHM/FWTM. This quantity is displayed in Fig. 17 for all cases reported in Table 6. For an ideal Gaussian distribution the ratio FWHM/FWTM is equal to 0.549. As it can be observed in Fig. 17, Gaussian photopeak distributions are obtained mostly for short half-lives of $t_{1/2} \lesssim 1$ ps, except for the thick beryllium target at short target–array distances, where FWHM/FWTM $\lesssim 0.4$. Thus, for $t_{1/2} \lesssim 1$ ps rather symmetric peaks and resolutions of 16–17 keV FWHM can be expected for measurements with the thin beryllium target, and 20–23 keV FWHM for the thick target at the short distance. The thick target at the large distance yields rather broad distributions with FWHM ≥ 35 keV. For $t_{1/2} \geq 10$ ps the ratio FWHM/FWTM becomes substantially smaller than 0.549, thus indicating the existence of tails in the reconstructed photopeak distribution, either towards higher or lower γ-ray energies. Therefore, this set-up is well suited for measuring half-lives of the order of few ps. Interestingly, the small value for FWHM/FWTM at 10 ps for the thick Be-target at the large distance reflects the prominent tail towards high γ-ray energy, which in combination with its small width of 8 keV FWHM (see Table 6) represents an ideal case for half-life measurement (see Section 9).

A remarkable improvement in the width of the reconstructed photopeak can be obtained if the value of the transition half-life is known, particularly for transitions with short lifetimes. Indeed, in these cases one can calculate the mean value for both, the reaction-product velocity and the z-position at de-excitation time, and use them for the Doppler correction. In order to illustrate this we choose the example of the 500 mg/cm^2 Be-target at 8.5 cm (see Fig. 16b). Table 7 shows the mean values of β and z at de-excitation time obtained from the MC-simulation.

As shown in Fig. 18, when instead of β_{at} and $z=0$, the mean values of Table 7 are used for the Doppler correction, one obtains rather symmetric distributions (at least for $t_{1/2} < 50$ ps), as well as an improvement in the width of the Doppler corrected photopeak ($\lesssim 20$ keV FWHM for all transitions with $t_{1/2} < 50$ ps). On the other hand, when the value of the half-life is unknown, one can apply a multiple Doppler correction, assuming different values for the lifetime, and implementing in each case the corresponding mean position and velocity values. This might lead to an improved Doppler corrected spectrum, as well as to an estimate of the transition lifetime. More precise methods for the measurement of the lifetime are reported in Section 9.
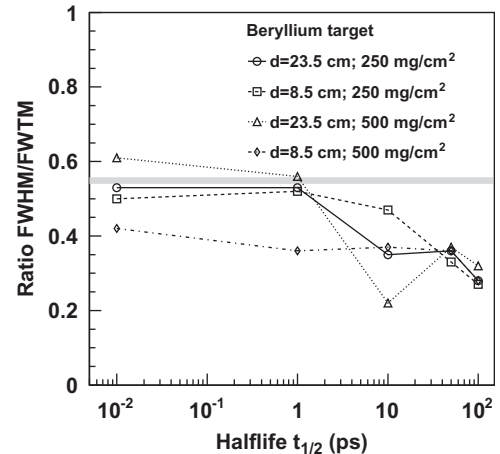

Fig. 17. Ratio between FWHM and FWTM as a function of the transition half-life for the different cases simulated with a beryllium target. The broad horizontal line indicates the ratio FWHM/FWTM for a Gaussian distribution.

Table 7
Mean β and z values at de-excitation time for the 500 mg/cm^2 thick Be-target.

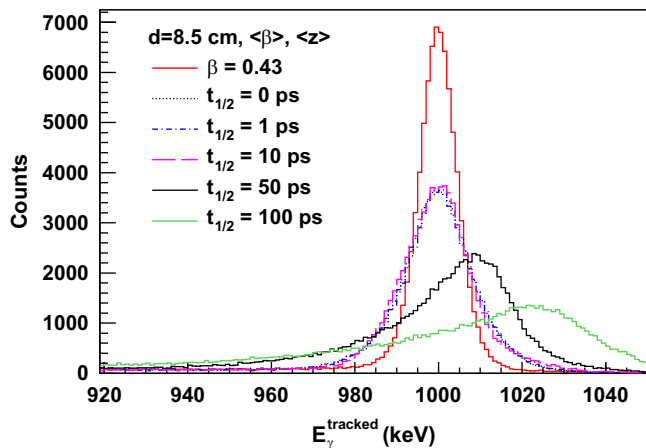| τ (ps)	$\langle\beta\rangle$	$\langle z\rangle$ (mm)
0	0.401	0.0
1	0.397	0.2
10	0.380	1.8
50	0.371	8.8
100	0.369	17.5

Fig. 18. Same as Fig. 16b, but assuming that the transition half-life is known, which allows one to use the mean velocity $\langle\beta\rangle$ and the mean position $\langle z\rangle$ values at de-excitation time for the Doppler correction of the spectrum.

8.2. Heavy secondary target

For secondary samples made of gold, the intrinsic stopping power is higher than for beryllium, but the distance which the reaction product needs to travel in order to cross the sample is a factor of 10 smaller. For gold targets one obtains the spectra shown in Fig. 19 and in Fig. 20, for thicknesses of 250 mg/cm^2 and 500 mg/cm^2, respectively. The values for the energy resolution are listed in Table 8. For half-lives between 1 ps and 10 ps, for both target thicknesses most of the decays happen after traversing the target, thus yielding in both cases a rather thin distribution, which is only 1–4 keV broader than the ideally thin target case. This applies for both target–array distances of 23.5 cm and 8.5 cm. For shorter ($t_{1/2} < 1$ ps) or larger ($t_{1/2} > 10$ ps) half-lives, the width of the reconstructed peak increases by a factor of two, or more, owing to the aforementioned effects of larger uncertainties on β and on z-position at de-excitation time, respectively.

The ratio between FWHM and FWTM is represented in Fig. 21 for the gold target. All transitions with $t_{1/2} \sim 10$ ps, regardless of target thickness and position, show both a rather Gaussian shape with FWHM/FWHTM ~ 0.5 and a narrow width of 7–14 keV FWHM. For $t_{1/2} = 1$ ps the narrow width of 7 keV FWHM obtained for the 500 mg/cm^2 Be-target at 23.5 cm in combination with the small ratio FWHM/FWHTM ~ 0.2 indicates that this set-up is well suited for measuring half-lives of $\sim$ ps.

In summary, the attainable resolution at 1 MeV ranges between 7 keV and $\gtrsim 20$ keV. The precise value depends sensitively on the projectile kinematics and characteristics (its atomic and mass numbers), target thickness and material, the target–array distance and the lifetime of the expected nuclear transition. In this respect, for the successful plan of in-flight experiments at GSI-FRS, it becomes useful to perform dedicated MC simulations in advance of the experimental work, which include all these ingredients in a realistic way. This should allow one to optimize
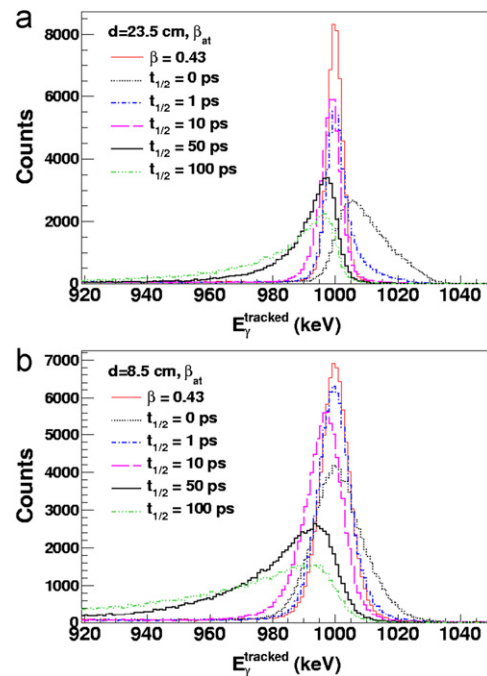

Fig. 19. Same as Fig. 15, but for a gold target with a thickness of 250 mg/cm^2.
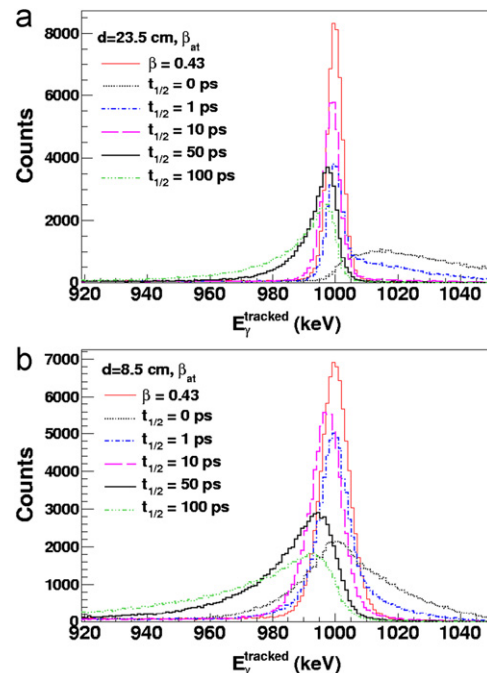

Fig. 20. Same as Fig. 19, but for a gold target with a thickness of 500 mg/cm^2.

the experimental set-up, and also select the secondary ion beam and the kinematics, which are best suited for the aim of each particular measurement.

9. Lifetime measurement

As described in Ref. [51], there are essentially two effects that can be exploited in order to evaluate the effective transition lifetime from the shape of the corresponding peak. The first one makes use of the dependence of the emission point along the beam axis z with the transition half-life. The second one uses the

Table 8
Estimated γ-ray energy resolution simulated for de-excitations from a reaction on a gold target for several assumptions of the target thickness and the half-life of the transition.

$t_{1/2}$ (ps)	RESOLUTION FWHM [FWTM] (keV)			
	250 mg/cm²		500 mg/cm²	
	$d=23.5$ cm	$d=8.5$ cm	$d=23.5$ cm	$d=8.5$ cm
0	19 [35]	18 [37]	42 [78]	28 [77]
1	8 [19]	12 [25]	7 [34]	12 [32]
10	8 [17]	14 [29]	7 [14]	13 [25]
50	12 [33]	27 [73]	10 [26]	21 [57]
100	17 [56]	42 [151]	14 [42]	34 [104]
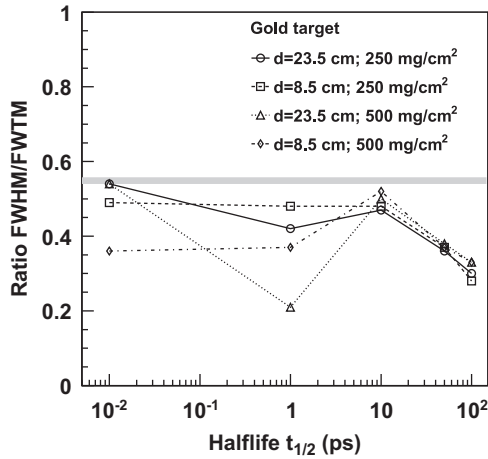
Fig. 21. Ratio between FWHM and FWTM as a function of the transition half-life for the different cases simulated with a gold target. The broad horizontal line indicates the ratio FWHM/FWTM for a Gaussian distribution.

emission during the slow-down process. In this case, the asymmetry of the reconstructed peak is larger at small angles.

The high position resolution, together with the possibility to work at target–array distance of 8.5–23.5 cm, makes AGATA particularly well suited for both methods.

9.1. Large lifetimes via centroid-shift at large angles

As described above in Section 8, this effect arises from the dependence of the average distance from reaction to de-excitation on the value of the lifetime. Whereas for short lifetimes ($t_{1/2} \lesssim 1$ ps) the excited nucleus de-excites inside the target and, in good approximation, the mean de-excitation position along the beam axis corresponds to $z \sim 0$, for large lifetimes (~ 100 ps) this value is shifted towards higher distances $z \sim$ cm, thus being the real emission angle larger than the one obtained from the $z=0$ assumption used for the Doppler reconstruction, and shifting the centroid of the γ-ray peak towards lower energy. Since the velocity of the products at $\beta \sim 0.4$ is of the order of 0.1–0.2 mm/ps, this effect is more evident for lifetime values of few tens to hundreds of ps. The best angular range to exploit this effect corresponds to angles, such that $\cos(\theta_\gamma) = \beta$ [51]. Thus, for the typical relativistic beam velocities of GSI-FRS $\beta = 0.43$, $\theta_\gamma \sim 65°$ and, as shown in Fig. 13, the optimal AGATA configurations for covering such angles are those for target–array distances of 8.5–13.5 cm. The peak centroid-shift effects e.g. for a 250 mg/cm² Be target at 8.5 cm become evident in the spectra shown in Fig. 15b. The systematics of this shift with the half-life are shown in

Fig. 22, which demonstrates that half-lives in the range of 10–100 ps can be derived via this method.

The shape of these spectra (Fig. 15b) is dominated by the centroid-shift ($z > 0$) effect because of the subtended angle and the range of half-lives. However, a component towards high energy is still noticeable for short half-lives $t_{1/2} \lesssim 1$ ps. The high angular resolution of AGATA can be utilized here in order to disentangle the $z > 0$ effect of interest (which shifts the peak centroid towards lower values) from the effect of de-excitation during deceleration (which shifts the peak centroid towards higher values). This is achieved by applying an angular cut at $64° < \theta_\gamma < 66°$, resulting in the distributions shown in Fig. 23, which are fully dominated by the $z > 0$ effect.
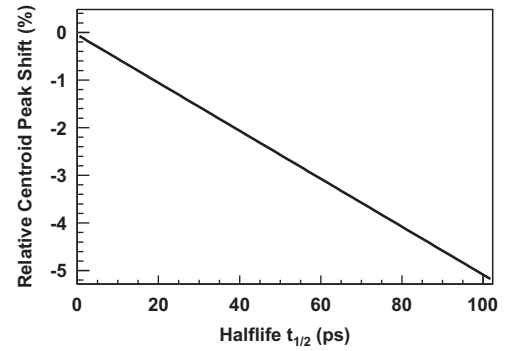

Fig. 22. Systematics of the peak centroid shift for a 250 mg/cm² Be-target at 8.5 cm from the array (see text for details).
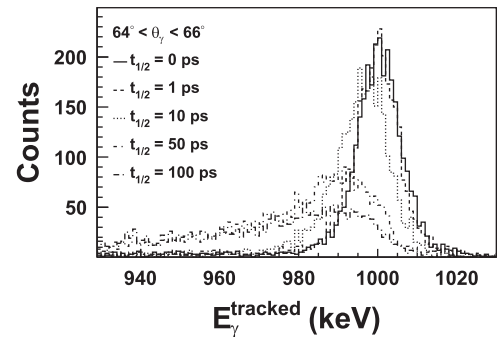

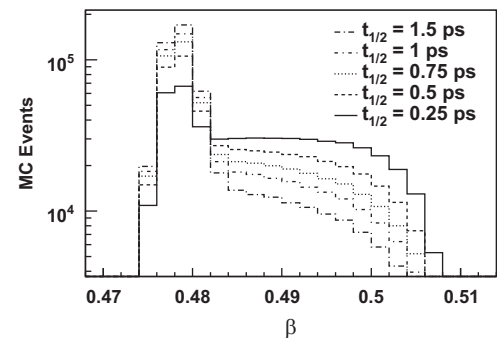**Fig. 23.** Line shape reconstructed for the 250 mg/cm² Be-target at 8.5 cm applying an angular cut of $65 \pm 1°$.

Fig. 24. β-Value at de-excitation time of the reaction product in a gold target 500 mg/cm² thick for an initial beam energy of 150 MeV/u.

9.2. Small lifetimes via doppler shift attenuation method

For lifetimes of few ps the Doppler-reconstructed photopeak typically shows two components. One of them is centred at the proper energy $E_{\gamma,\circ}$, and arises from de-excitations happening shortly after the target, where the velocity remains constant and can be measured. The second contribution extends towards
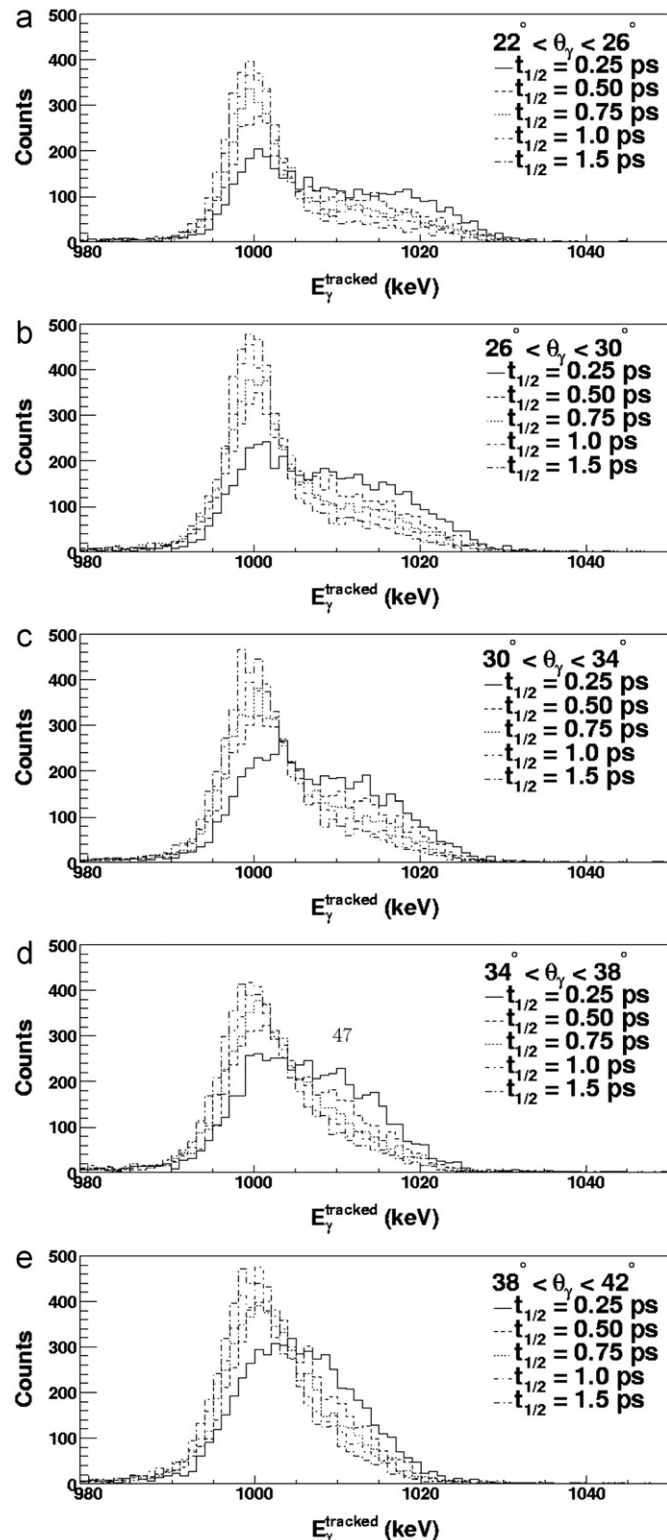

Fig. 25. Doppler reconstructed spectra for several angular slices. Half-lives between 0.25 and 1.5 ps have been simulated. See text for details.

$E_\gamma > E_{\gamma,\circ}$, and is due to de-excitations inside the target, where $\beta > \beta_{at}$. This tail towards high energy becomes more prominent at small angles (see Eq. (1)). Indeed, at small angles θ_γ the shape of the Doppler corrected spectrum reflects the pattern of the velocity distribution at de-excitation time. This effect is illustrated in Fig. 24 for the example described in Section 8, now assuming half-life values between 0.25 ps and 1.5 ps, a gold target of 500 mg/cm^2 and a secondary beam energy of 150 MeV/u. The signature of the lifetime in the value of β at the moment of de-excitation is further reflected in the Doppler reconstructed spectra, as it can be appreciated in Fig. 25. The latter shows the photopeak distributions for several angular slices ($\Delta\theta_\gamma = 4^\circ$) at forward angles between 22° and 42°.

Thus, the fine angular resolution of AGATA allows one to measure accurately the angular evolution of the Doppler corrected photopeak. By comparing the systematics of this trend versus detailed MC-simulations one can determine the lifetime value for rather fast nuclear transitions, between approximately 200 fs and 2 ps.

10. Summary and conclusions

The R&D and the final conceptual design of AGATA for experiments at GSI-FRS has been presented. The solution proposed requires the development of AGATA double cluster detectors, thus aiming at a full optimization of the tracking array for in-beam γ-ray spectroscopy experiments at this facility. A systematic study based on Monte Carlo simulations is reported, which comprises several parameters such as the target–array distance, number of detectors available, energy of the γ-ray transition and influence of passive elements. Thus, for relativistic beams with $\beta = 0.43$, using an AGATA configuration of 5 double- and 5 triple-cluster detectors, photopeak efficiencies between 6% and 11% can be obtained for $E_{\gamma,\circ} = 1$ MeV (energy at rest), and target–array distances of 23.5 cm and 8.5 cm, respectively. These values become 11% and 17%, respectively, when five additional triple cluster detectors are added. The energy resolution attainable in Doppler corrected spectra depends on the particular experiment details and it seems to be, in most cases, dominated by energy loss effects in the secondary target and by the half-life of the expected transition. In this respect, it is recommended to carry out dedicated simulations in order to obtain realistic values for each particular experiment. As follow-up of a previous publication [51], the application of lineshape effects measurable with AGATA for the determination of transition half-lives has been investigated. Using the AGATA response at large angles $\theta \sim 65^\circ$, and at short angles $\theta \sim 20$–30°, our simulation shows that it is possible to determine the value of half-lives of 10–100 ps, and 0.1–1 ps, respectively.

References

[1] F.A. Beck, Progress in Particle and Nuclear Physics 28 (1992) 443.
[2] I.Y. Lee, Nuclear Physics A 520 (December) (1990) 641.
[3] R.M. Diamond (Ed.). High-Spin Gamma-Ray Spectroscopy, March 1984.

[4] P.J. Twin, P.J. Nolan, R. Aryaeinejad, D.J.G. Love, A.H. Nelson, A. Kirwan, Nuclear Physics A 409 (November) (1983) 343.
[5] O. Moller, A. Dewald, P. Petkov, B. Saha, A. Fitzler, K. Jessen, D. Tonev, T. Klug, S. Heinze, J. Jolie, P. von Brentano, D. Bazzacco, C.A. Ur, E. Farnea, M. Axiotis, S. Lunardi, G. de Angelis, D.R. Napoli, N. Marginean, T. Martinez, M.A. Caprio, R.F. Casten, Physical Review C 74 (2006) 024313.
[6] P. Petkov, A. Dewald, O. Moller, B. Saha, A. Fitzler, K. Jessen, D. Tonev, T. Klug, S. Heinze, J. Jolie, P. von Brentano, D. Bazzacco, C. Ur, E. Farnea, M. Axiotis, S. Lunardi, C. Rossi-Alvarez, G. de Angelis, D.R. Napoli, N. Marginean, T. Martinez, M. Caprio, R.F. Casten, Physical Review C 68 (2003) 034328.
[7] M.A. Caprio, N.V. Zamfir, R.F. Casten, C.J. Barton, C.W. Beausang, J.R. Cooper, A.A. Hecht, R. Krucken, H. Newman, J.R. Novak, N. Pietralla, A. Wolf, K.E. Zyromski, Physical Review C 66 (2002) 054310.
[8] Perspectives of Nuclear Physics in Europe, NuPECC Long Range Plan 2010. European Science Foundation, 2010.
[9] S. Akkoyun, A. Algora, B. Alikhani, F. Ameil, G. de Angelis, L. Arnold, A. Astier, A. Ataç, Y. Aubert, C. Aufranc, et al., Nuclear Instruments and Methods in Physics Research A 668 (March) (2012) 26.
[10] M.A. Deleplanque, I.Y. Lee, K. Vetter, G.J. Schmid, F.S. Stephens, R.M. Clark, R.M. Diamond, P. Fallon, A.O. Macchiavelli, Nuclear Instruments and Methods in Physics Research A 430 (July) (1999) 292.
[11] F. Camera, AGATA: the European HPGe tracking array, in: A.J. Kreiner, O. Civitarese (Eds.), VI Latin American Symposium on Nuclear Physics and Applications, American Institute of Physics Conference Series, vol. 884, February 2007, pp. 97–102.
[12] E. Ince, E. Farnea, A. Latina, M.N. Erduran, Realistic simulations of the AGATA demonstrator+PRISMA spectrometer, in: I. Boztosun, A.B. Balantekin (Eds.), American Institute of Physics Conference Series, American Institute of Physics Conference Series, vol. 1072, November 2008, pp. 273–276.
[13] E. Farnea, The AGATA demonstrator array at Laboratori Nazionali di Legnaro: status of the project, in: M. Milin, T. Niksic, S. Szilner, D. Vretenar (Eds.), American Institute of Physics Conference Series, American Institute of Physics Conference Series, vol. 1165, August 2009, pp. 390–393.
[14] The Agata Collaboration, E. Farnea, F. Recchia, D. Bazzacco, T. Kröll, Z. Podolyák, B. Quintana, A. Gadea, The AGATA Collaboration, Nuclear Instruments and Methods in Physics Research A 621 (September) (2010) 331.
[15] The Agata, Prisma Collaborations, E. Ince, M.N. Erduran, E. Farnea, A. Latina, G. Pollarolo, The AGATA and PRISMA Collaborations, Nuclear Instruments and Methods in Physics Research A 622 (October) (2010) 107.
[16] A. Al-Adili, Simulations of Doppler Effects in Nuclear Reactions for AGATA Commissioning Experiments. ArXiv e-prints, September 2009.
[17] P. Reiter, B. Bruyneel, J. Eberth, H. Hess, G. Pascovici, N. Warr, A. Wiens, H.-G. Thomas, The new position sensitive triple cluster detector For AGATA, in: J. Jolie, A. Zilges, N. Warr, A. Blazhev (Eds.), American Institute of Physics Conference Series, American Institute of Physics Conference Series, vol. 1090, January 2009, pp. 97–101.
[18] L. Nelson, M.R. Dimmock, A.J. Boston, H.C. Boston, J.R. Cresswell, P.J. Nolan, I. Lazarus, J. Simpson, P. Medina, C. Santos, C. Parisel, Nuclear Instruments and Methods in Physics Research A 573 (April) (2007) 153.
[19] H.C. Boston, J.R. Cresswell, M.R. Dimmock, L. Nelson, P.J. Nolan, S. Rigby, I. Lazarus, J. Simpson, P. Medina, C. Santos, C. Parisel, The AGATA Collaboration, Nuclear Instruments and Methods in Physics Research B 261 (August) (2007) 1098.
[20] A.J. Boston, M.R. Dimmock, C. Unsworth, H.C. Boston, R.J. Cooper, A.N. Grint, L.J. Harkness, I.H. Lazarus, M. Jones, P.J. Nolan, D.C. Oxley, J. Simpson, M. Slee, Performance of an AGATA asymmetric detector, in: I. Boztosun, A.B. Balantekin (Eds.), American Institute of Physics Conference Series, vol. 1072, November 2008, pp. 130–135.
[21] C. Unsworth, A.J. Boston, H.C. Boston, S. Colosimo, J. Cresswell, M.R. Dimmock, F. Filmer, D. Judson, S. Moon, P.J. Nolan, M.J. Norman, M. Slee, Characterisation of an asymmetric AGATA detector, in: Society of Photo-Optical Instrumentation Engineers (SPIE) Conference Series, vol. 7449, August 2009.
[22] M.R. Dimmock, A.J. Boston, J.R. Cresswell, I. Lazarus, P. Medina, P. Nolan, C. Parisel, C. Santos, J. Simpson, C. Unsworth, IEEE Transactions on Nuclear Science 56 (August) (2009) 2415.
[23] M.R. Dimmock, A.J. Boston, H.C. Boston, J.R. Cresswell, L. Nelson, P.J. Nolan, C. Unsworth, I.H. Lazarus, J. Simpson, IEEE Transactions on Nuclear Science NS-56 (June) (2009) 1593.
[24] The Agata Collaboration, A.J. Boston, M.R. Dimmock, C. Unsworth, H.C. Boston, R.J. Cooper, A.N. Grint, L.J. Harkness, I.H. Lazarus, M. Jones, P.J. Nolan, D.C. Oxley, J. Simpson, M. Slee, The AGATA Collaboration, Nuclear Instruments and Methods in Physics Research A, 604 (June) (2009) 48.
[25] A.J. Boston, M.R. Dimmock, C. Unsworth, H.C. Boston, R.J. Cooper, A.N. Grint, L.J. Harkness, I.H. Lazarus, M. Jones, P.J. Nolan, D.C. Oxley, J. Simpson, M. Slee, Status and performance of an AGATA asymmetric detector, in: D. Dashdorj, U. Agvaanluvsan, G.E. Mitchell (Eds.), American Institute of Physics Conference Series, vol. 1109, March 2009, pp. 38–43.
[26] M. Bellato, L. Berti, D. Bortolato, P.J. Coleman-Smith, P. Edelbruck, X. Grave, R. Isocrate, I. Lazarus, D. Linget, P. Medina, C. Oziol, G. Rampazzo, C. Santos, B. Travers, A. Triossi, IEEE Transactions on Nuclear Science NS55 (2008) 91.
[27] F. Zocca, A. Pullia, D. Bazzacco, G. Pascovici, IEEE Transactions on Nuclear Science NS-56 (August) (2009) 2384.
[28] F. Recchia, D. Bazzacco, E. Farnea, A. Gadea, R. Venturelli, T. Beck, P. Bednarczyk, A. Buerger, A. Dewald, M. Dimmock, G. Duchêne, J. Eberth, T. Faul, J. Gerl, R. Gernhaeuser, K. Hauschild, A. Holler, P. Jones, W. Korten, T. Kröll, R. Krücken, N. Kurz, J. Ljungvall, S. Lunardi, P. Maierbeck, D. Mengoni, J. Nyberg, L. Nelson, G. Pascovici, P. Reiter, H. Schaffner, M. Schlarb, T. Steinhardt, O. Thelen, C.A. Ur, J.J. Valiente Dobon, D. Weißhaar, Nuclear Instruments and Methods in Physics Research A 604 (June) (2009) 555.
[29] For The Agata Collaboration, F. Recchia, D. Bazzacco, E. Farnea, R. Venturelli, S. Aydin, G. Suliman, C.A. Ur, For the AGATA Collaboration, Nuclear Instruments and Methods in Physics Research A 604 (June) (2009) 60.
[30] For The Agata Collaboration, A. Wiens, H. Hess, B. Birkenbach, B. Bruyneel, J. Eberth, D. Lersch, G. Pascovici, P. Reiter, H.-G. Thomas, and for the AGATA Collaboration, Nuclear Instruments and Methods in Physics Research A 618 (June) (2010) 223.
[31] F. Recchia, Journal of Physics: Conference Series 205 (January (1)) (2010) 012045.
[32] F. Recchia, Acta Physica Polonica B 38 (April) (2007) 1297.
[33] P.A. Söderström, A. Al-Adili, J. Nyberg, F. Recchia, E. Farnea, A. Gadea, Gamma tracking with the AGATA detector, in: Proceedings of the 17th International Workshop on Vertex Detectors, July 28–August 1, 2008. Utö Island, Sweden. Published online at ⟨href="http://pos.sissa.it/cgi-bin/reader/conf.cgi?confid=68"⟩ ⟨http://pos.sissa.it/cgi-bin/reader/conf.cgi?confid=68⟩, 2008, p. 40.
[34] A. Ataç, A. Kaşkaş, S. Akkoyun, M. şenyiğit, T. Hüyük, S.O. Kara, J. Nyberg, Nuclear Instruments and Methods in Physics Research A 607 (August) (2009) 554.
[35] The Agata Collaboration, M. Doncel, F. Recchia, B. Quintana, A. Gadea, E. Farnea, and The AGATA Collaboration. Nuclear Instruments and Methods in Physics Research A 622 (October) (2010) 614.
[36] M. Doncel, F. Recchia, A. Gadea, E. Farnea, B. Quintana, Compton imaging capabilities of AGATA for background rejection, in: J.A. Caballero, C.E. Alonso, M.V. Andrés, J.E. García Ramos, F. Pérez-Bernal (Eds.), American Institute of Physics Conference Series, vol. 1231, April 2010, pp. 213–214.
[37] The Agata, Prisma Collaborations, A. Gadea, E. Farnea, J.J. Valiente-Dobón, B. Million, D. Mengoni, D. Bazzacco, F. Recchia, A. Dewald, T. Pissulla, W. Rother, G. de Angelis, A. Austin, S. Aydin, S. Badoer, M. Bellato, G. Benzoni, L. Berti, R. Beunard, B. Birkenbach, E. Bissiato, N. Blasi, C. Boiano, D. Bortolato, A. Bracco, S. Brambilla, B. Bruyneel, E. Calore, F. Camera, A. Capsoni, J. Chavas, P. Cocconi, S. Coelli, A. Colombo, D. Conventi, L. Costa, L. Corradi, A. Corsi, A. Cortesi, F.C.L. Crespi, N. Dosme, J. Eberth, S. Fantinel, C. Fanin, E. Fioretto, C. Fransen, A. Giaz, A. Gottardo, X. Grave, J. Grebosz, R. Griffiths, E. Grodner, M. Gulmini, T. Habermann, C. He, H. Hess, R. Isocrate, J. Jolie, P. Jones, A. Latina, E. Legay, S. Lenzi, S. Leoni, F. Lelli, D. Lersch, S. Lunardi, G. Maron, R. Menegazzo, C. Michelagnoli, P. Molini, G. Montagnoli, D. Montanari, O. Möller, D. R. Napoli, R. Nicolini, M. Ozille, G. Pascovici, R. Peghin, M. Pignanelli, V. Pucknell, A. Pullia, L. Ramina, G. Rampazzo, M. Rebeschini, P. Reiter, S. Riboldi, M. Rigato, C. Rossi Alvarez, D. Rosso, G. Salvato, J. Strachan, E. Sahin, F. Scarlassara, J. Simpson, A.M. Stefanini, O. Stezowski, F. Tomasi, N. Toniolo, A. Triossi, M. Turcato, C.A. Ur, V. Vandone, R. Venturelli, F. Veronese, C. Veyssiere, E. Viscione, O. Wieland, A. Wiens, F. Zocca, A. Zucchiatti, Nuclear Instruments and Methods in Physics Research A 654 (October) (2011) 88.
[38] J. Gerl, Acta Physica Polonica B 40 (March) (2009) 767.
[39] H. Geissel, H. Weick, M. Winkler, M. Münzenberg, V. Chichkine, M. Yavor, T. Aumann, K.H. Behr, M. Böhmer, A. Brünle, K. Burkard, J. Benlliure, D. Cortina-Gil, L. Chulkov, A. Dael, J.-E. Ducret, H. Emling, B. Franczak, J. Friese, B. Gastineau, J. Gerl, R. Gernhäuser, M. Hellström, B. Jonson, J. Kojouharova, R. Kulessa, B. Kindler, N. Kurz, B. Lommel, W. Mittig, G. Moritz, C. Mühle, J.A. Nolen, G. Nyman, P. Roussell-Chomaz, C. Scheidenberger, K.-H. Schmidt, G. Schrieder, B.M. Sherrill, H. Simon, K. Sümmerer, N.A. Tahir, V. Vysotsky, H. Wollnik, A.F. Zeller, Nuclear Instruments and Methods in Physics Research B 204 (May) (2003) 71.
[40] M. Winkler, H. Geissel, H. Weick, B. Achenbach, K.-H. Behr, D. Boutin, A. Brünle, M. Gleim, W. Hüller, C. Karagiannis, A. Kelic, B. Kindler, E. Kozlova, H. Leibrock, B. Lommel, G. Moritz, C. Mühle, G. Münzenberg, C. Nociforo, W. Plass, C. Scheidenberger, H. Simon, K. Sümmerer, N.A. Tahir, A. Tauschwitz, M. Tomut, J.S. Winfield, M. Yavor, Nuclear Instruments and Methods in Physics Research B 266 (October) (2008) 4183.
[41] P. Bednarczyk, J. Grębosz, M. Kmiecik, A. Maj, W. Męczyński, J. Styczeń, C. Domingo-Pardo, P. Doornenbal, J. Gerl, M. Górska, H.J. Wollersheim, J. Jolie, P. Reiter, A. Bracco, F. Camera, Acta Physica Polonica B 41 (January) (2010) 505.
[42] H. Geissel, P. Armbruster, K.H. Behr, A. Brünle, K. Burkard, M. Chen, H. Folger, B. Franczak, H. Keller, O. Klepper, B. Langenbeck, F. Nickel, E. Pfeng, M. Pfützner, E. Roeckl, K. Rykaczewski, I. Schall, D. Schardt, C. Scheidenberger, K.-H. Schmidt, A. Schröter, T. Schwab, K. Sümmerer, M. Weber, G. Münzenberg, T. Brohm, H.-G. Clerc, M. Fauerbach, J.-J. Gaimard, A. Grewe, E. Hanelt, B. Knödler, M. Steiner, B. Voss, J. Weckenmann, C. Ziegler, A. Magel, H. Wollnik, J.P. Dufour, Y. Fujita, D.J. Vieira, B. Sherrill, Nuclear Instruments and Methods in Physics Research B 70 (August) (1992) 286.
[43] D. Rudolph, et al. LYCCA—The Lund York Cologne CAlorimeter. Technical Report, FAIR TAC HISPEC/DESPEC, 2010.
[44] H.J. Wollersheim, D.E. Appelbe, A. Banu, R. Bassini, T. Beck, F. Becker, P. Bednarczyk, K.-H. Behr, M.A. Bentley, G. Benzoni, C. Boiano, U. Bonnes, A. Bracco, S. Brambilla, A. Brunle, A. Burger, K. Burkard, P.A. Butler, F. Camera, D. Curien, J. Devin, P. Doornenbal, C. Fahlander, K. Fayz, H. Geissel, J. Gerl, M. Gorska, H. Grawe, J. Grebosz, R. Griffiths, G. Hammond, M. Hellstrom, J. Hoffmann, H. Hubel, J. Jolie, J.V. Kalben, M. Kmiecik, I. Kojouharov, R. Kulessa, N. Kurz, I. Lazarus, J. Li, J. Leske, R. Lozeva, A. Maj, S. Mandal, W. Meczynski, B. Million, G. Munzenberg, S. Muralithar, M. Mutterer,

P.J. Nolan, G. Neyens, J. Nyberg, W. Prokopowicz, V.F.E. Pucknell, P. Reiter, D. Rudolph, N. Saito, T.R. Saito, D. Seddon, H. Schaffner, J. Simpson, K.-H. Speidel, J. Styczen, K. Summerer, N. Warr, H. Weick, C. Wheldon, O. Wieland, M. Winkler, M. Zieblinski, Nuclear Instruments and Methods in Physics Research A 537 (February) (2005) 637.

[45] D. Bazzacco, MGT Code Developed Within the TMR Program 'Gamma-Ray Tracking Detectors'.

[46] C. Nochiforo, H. Weick, M. Winkler, private communication.

[47] J.A. Grau, Z.W. Grabowski, F.A. Rickey, P.C. Simms, R.M. Steffen, Physical Review Letters 32 (March) (1974) 677.

[48] P. Bednarczyk, J. Grębosz, A. Maj, M. Kmiecik, W. Męczyński, J. Styczeń, H.J. Wollersheim, J. Gerl, M. Górska, P. Reiter, A. Bracco, F. Camera, Acta Physica Polonica B 40 (March) (2009) 853.

[49] T.R. Saito, N. Saito, K. Starosta, J. Beller, N. Pietralla, H.J. Wollersheim, D.L. Balabanski, A. Banu, R.A. Bark, T. Beck, F. Becker, P. Bednarczyk, K.-H. Behr, G. Benzoni, P.G. Bizzeti, C. Boiano, A. Bracco, S. Brambilla, A. Brünle, A. Bürger, L. Caceres, F. Camera, F.C.L. Crespi, P. Doornenbal, A.B. Garnsworthy, H. Geissel, J. Gerl, M. Górska, J. Grebosz, G. Hagemann, J. Jolie, M. Kavatsyuk, O. Kavatsyuk, T. Koike, I. Kojouharov, N. Kurz, J. Leske, G. Lo Bianco, A. Maj, S. Mallion, S. Mandal, M. Maliage, T. Otsuka, C.M. Petrache, Z. Podolyak, W. Prokopowicz, G. Rainovski, P. Reiter, A. Richard, H. Schaffner, S. Schielke, G. Sletten, N.J. Thompson, D. Tonev, J. Walker, N. Warr, O. Wieland, Q. Zhong, Physics Letters B 669 (October) (2008) 19.

[50] P. Detistov, D.L. Balabanski, Z. Podolyak, Acta Physica Polonica B 38 (April) (2007) 1287.

[51] P. Doornenbal, P. Reiter, H. Grawe, T. Saito, A. Al-Khatib, A. Banu, T. Beck, F. Becker, P. Bednarczyk, G. Benzoni, A. Bracco, A. Bürger, L. Caceres, F. Camera, S. Chmel, F.C.L. Crespi, H. Geissel, J. Gerl, M. Górska, J. Greβosz, H. Hübel, M. Kavatsyuk, O. Kavatsyuk, M. Kmiecik, I. Kojouharov, N. Kurz, R. Lozeva, A. Maj, S. Mandal, W. Meczynski, B. Million, Z. Podolyák, A. Richard, N. Saito, H. Schaffner, M. Seidlitz, T. Striepling, J. Walker, N. Warr, H. Weick, O. Wieland, M. Winkler, H.J. Wollersheim, Nuclear Instruments and Methods in Physics Research A 613 (February) (2010) 218.